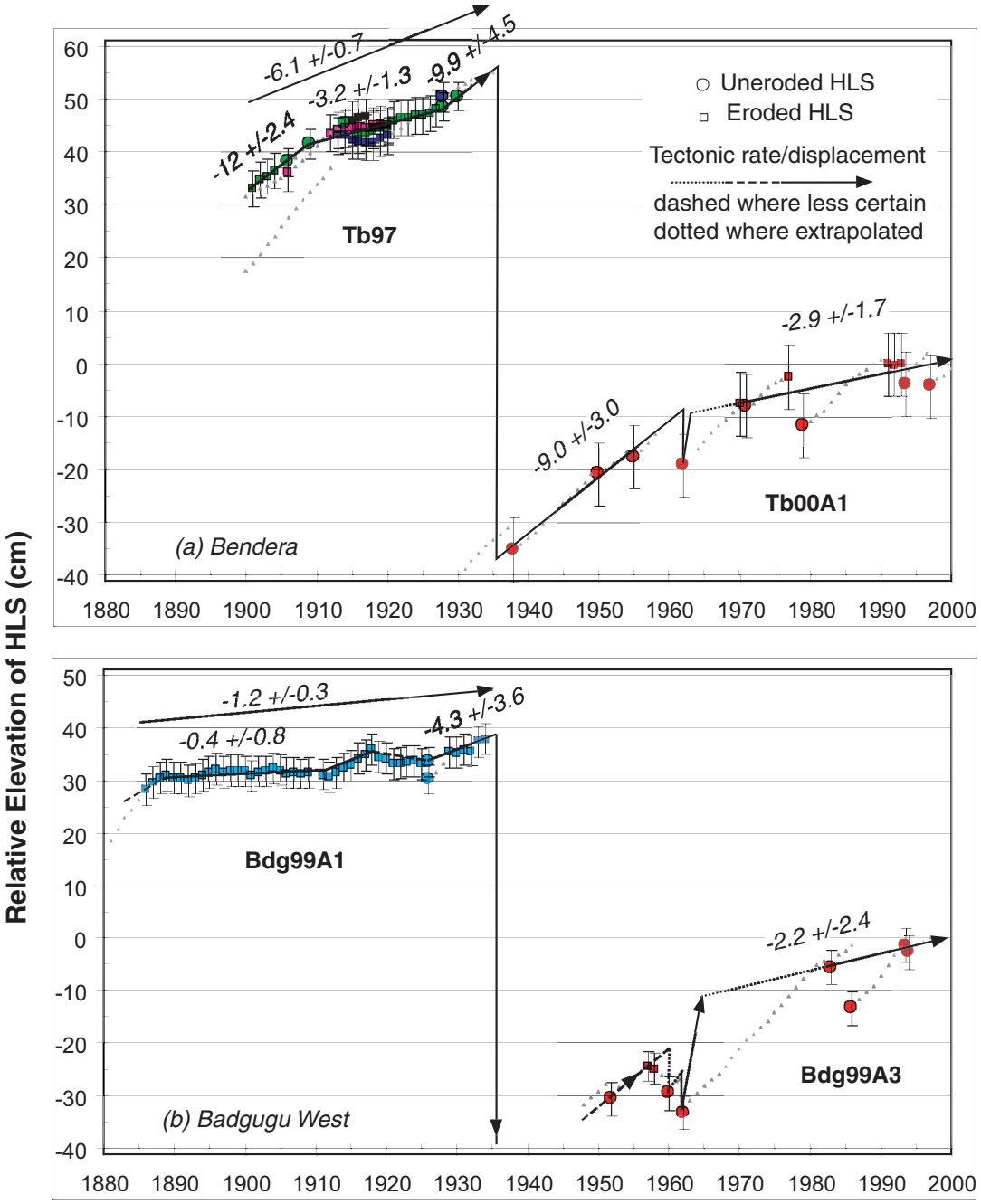

Figure 4.1 HLS histories of all sites, plotted with the aligned time scale and the same scaling of emergence and submergence relative to modern HLS. The 1935 event dominates the history. The 1962 event is the second largest event. The vertical deformation rates vary markedly from site to site and for different periods.

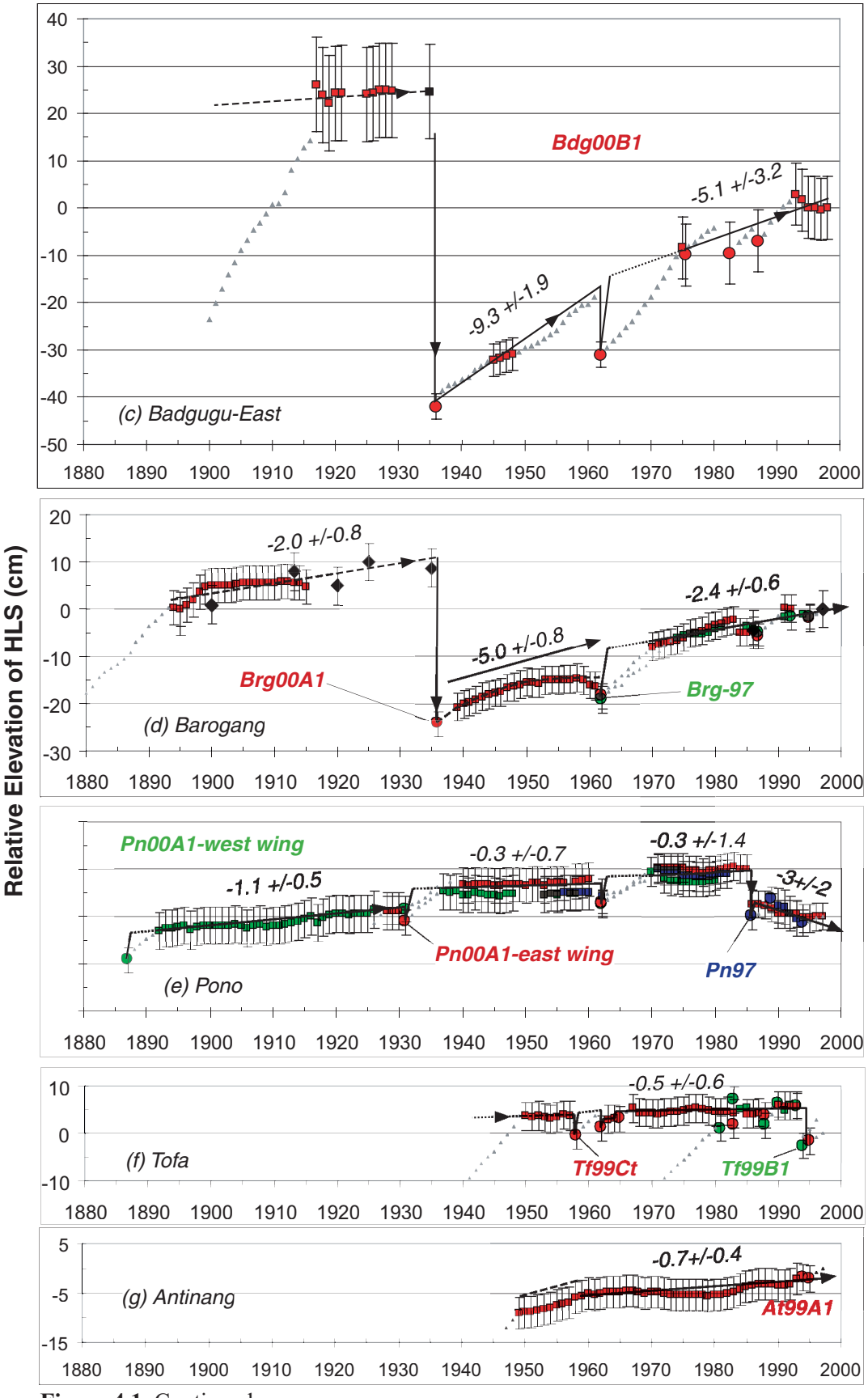

Figure 4.1 Continued ...

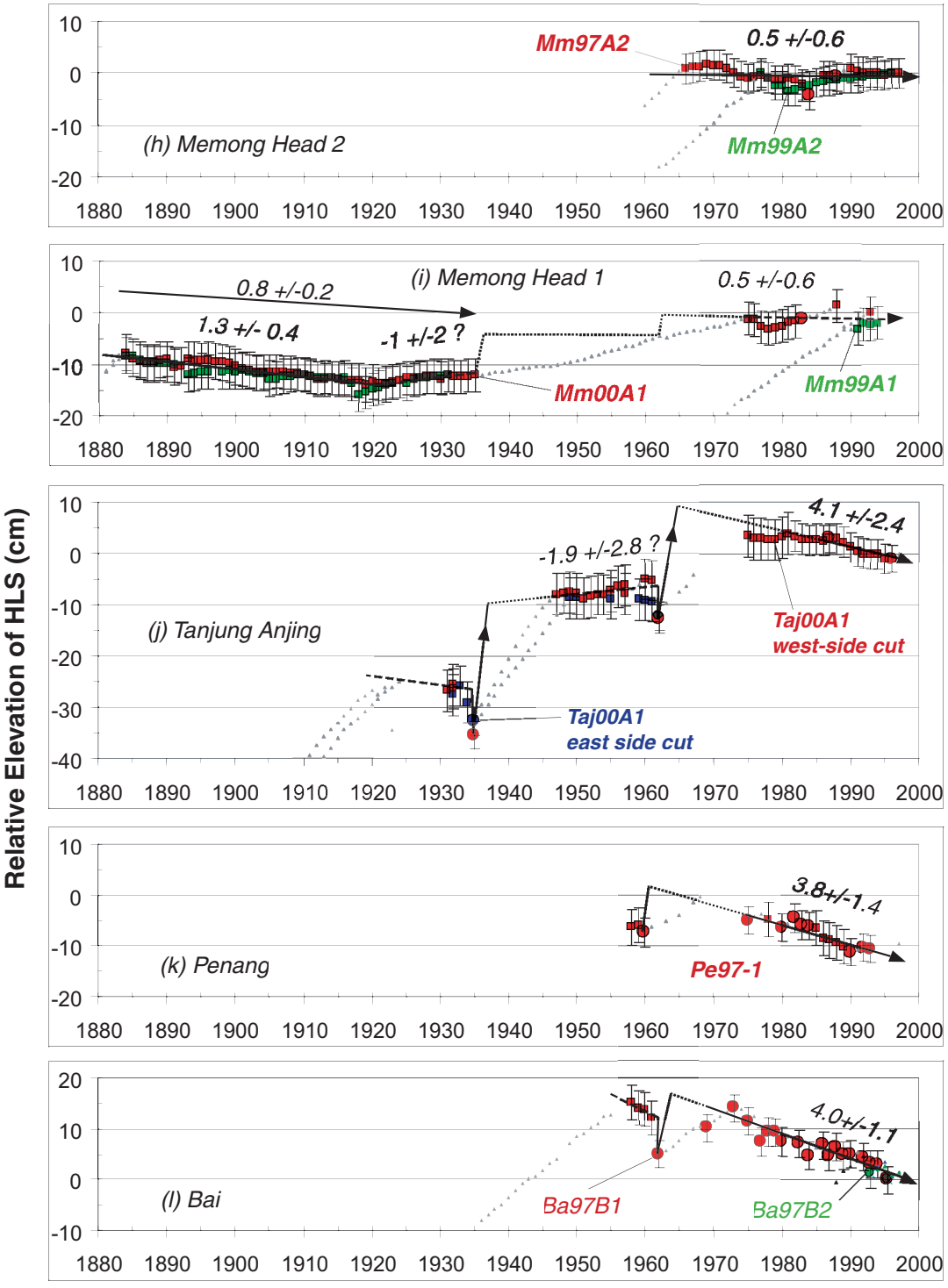

Figure 4.1 Continued ...

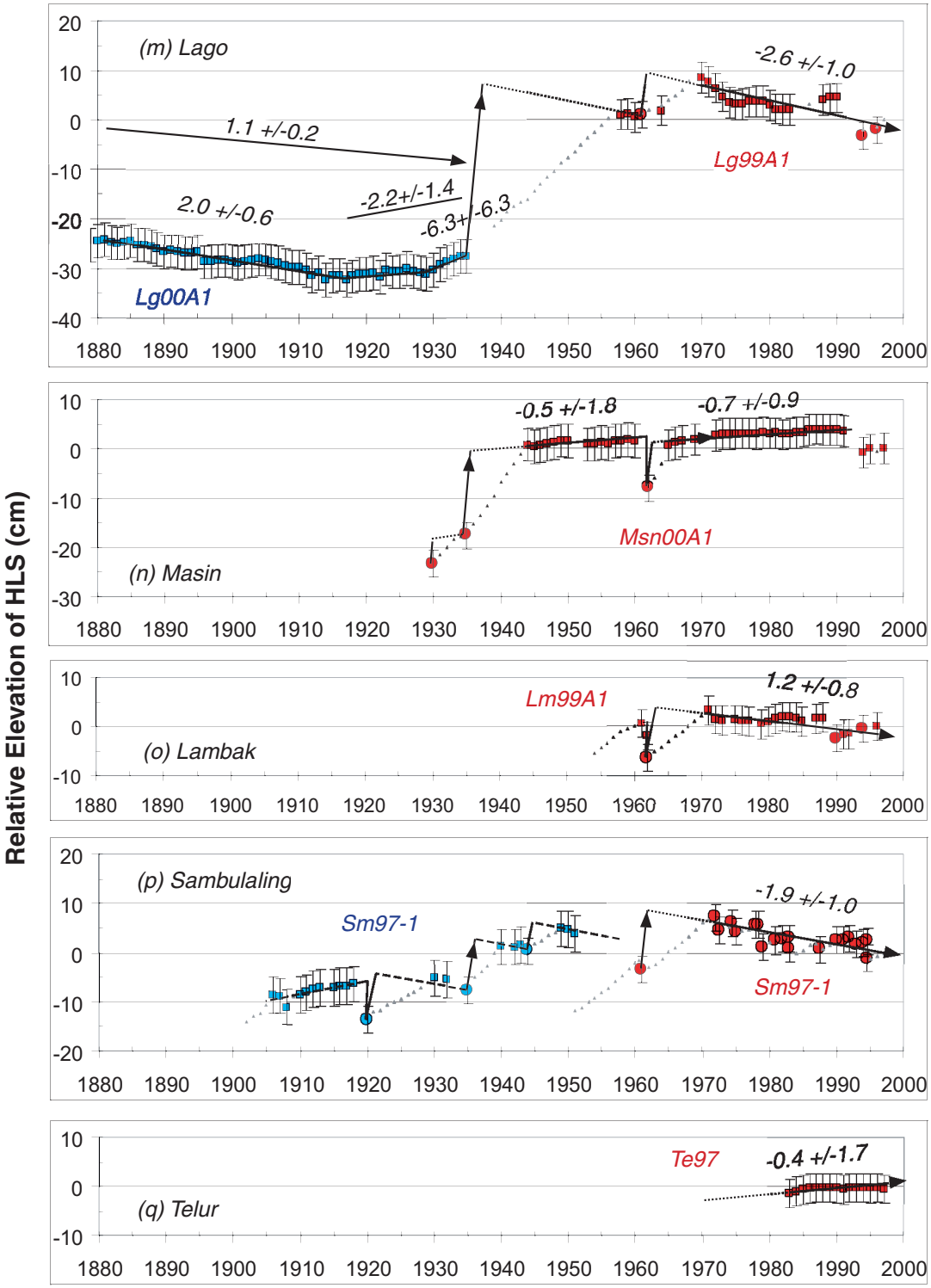

Figure 4.1 Continued ...

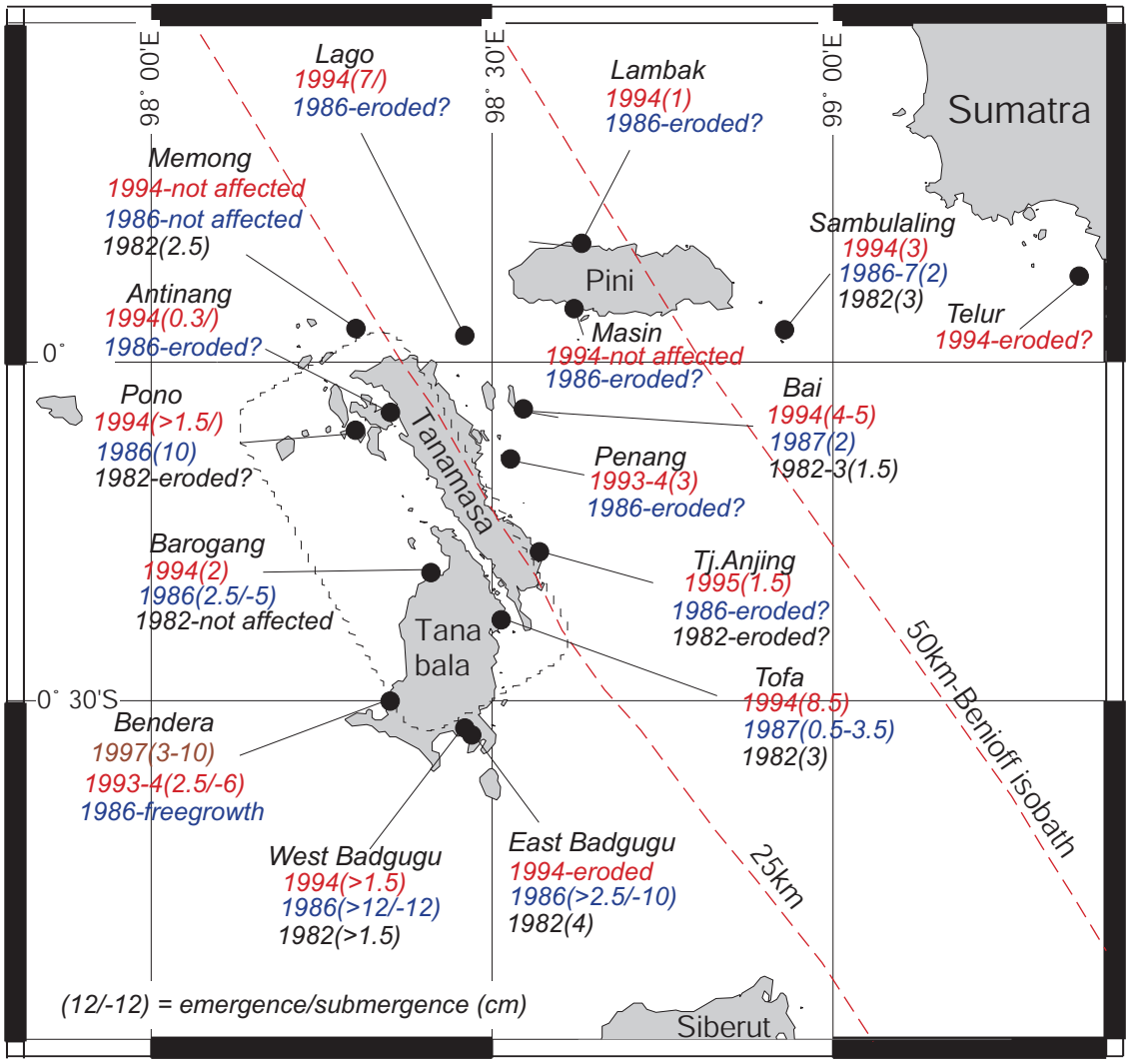

Figure 4.2 Non-tectonic HLS die-downs during ENSO and IOD (Indian Ocean Dipole) events. Values in the brackets are measured emergence/submergence (-) from the paleogeodetic records.

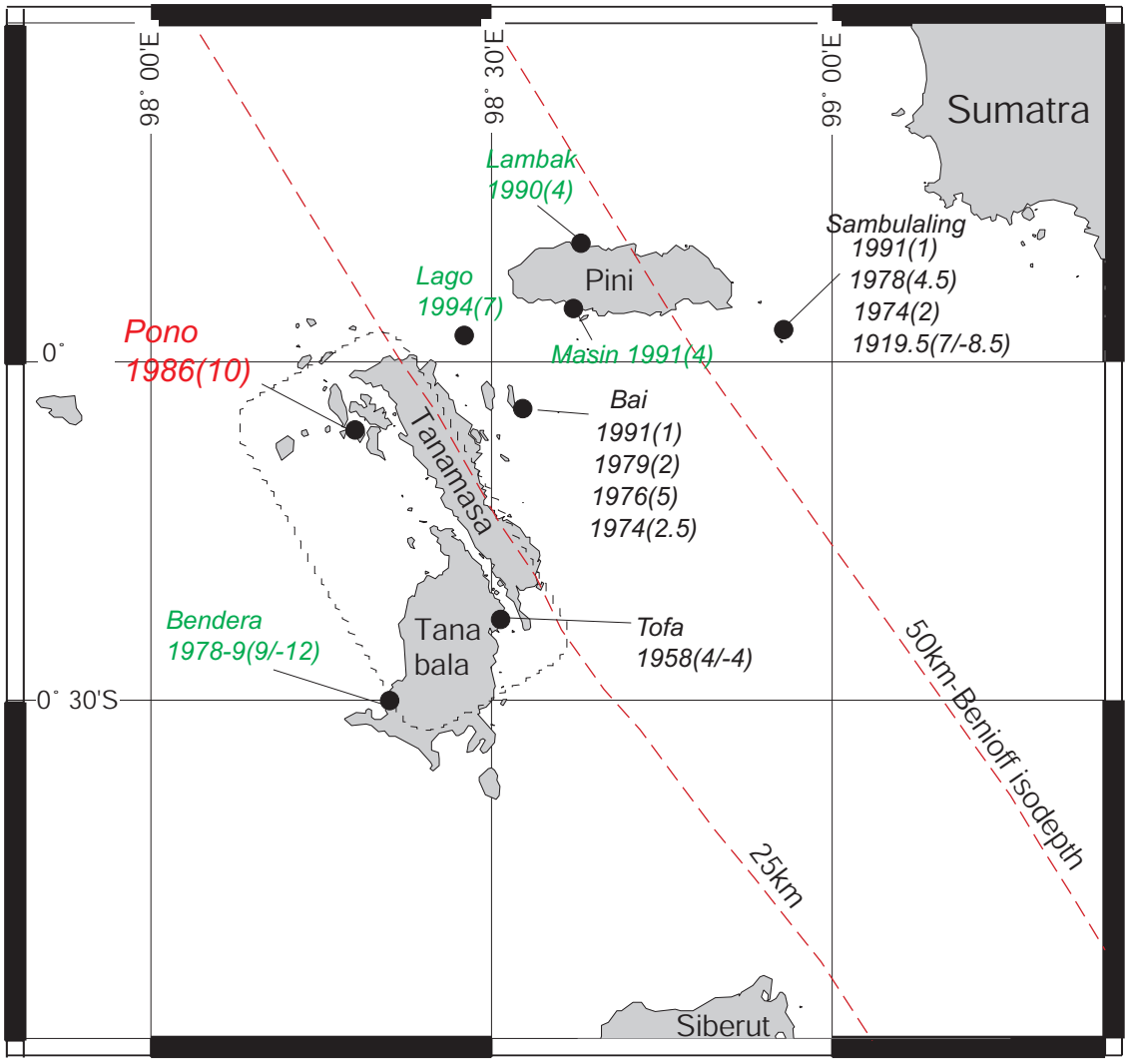

Figure 4.3 HLS die-downs that occurred locally. At the Pono site, the die-down in 1986 was probably of tectonic origin. The emergence/submergence episodes of 1978-9 at Bendera may reflect a very local tectonic event. At Masin and Lambak the die-down of ~1990 was possibly related to an earthquake event (Mw 5.2), but it may also be influenced by cyanide fishing. Sites with black letters probably experienced non-tectonic die-downs.

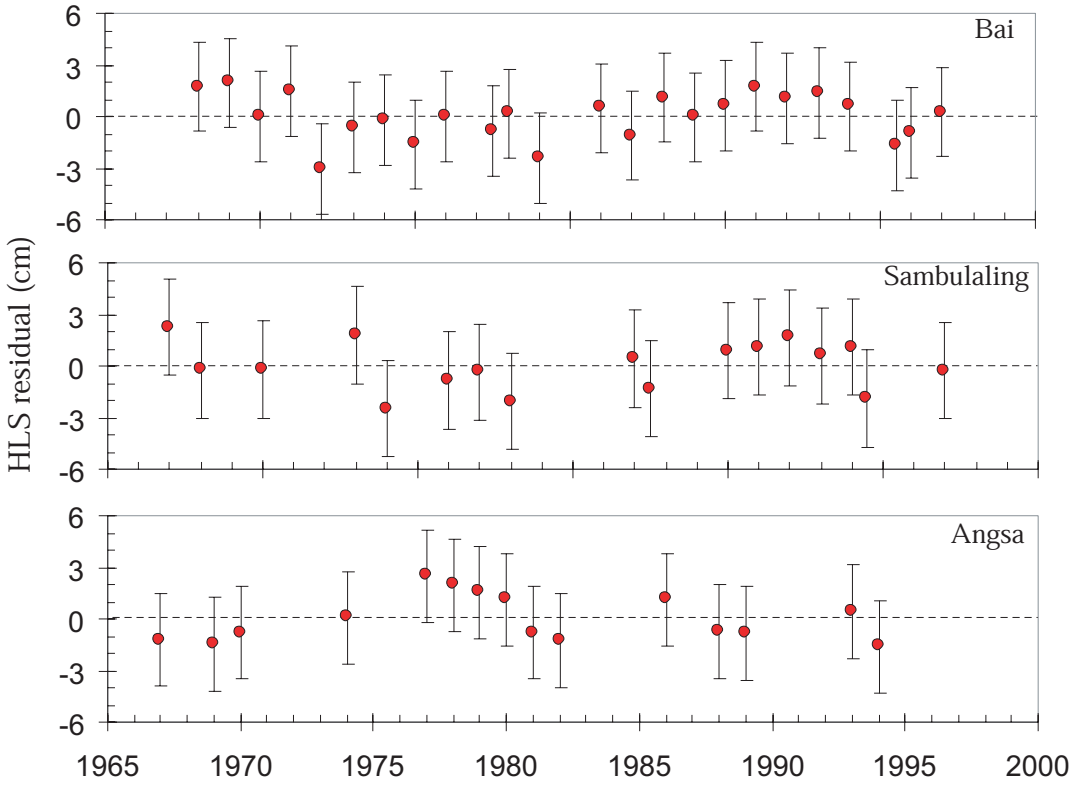

Figure 4.4a Three sites with particularly good HLS records allow calculation of uncertainties in rates of submergence/emergence due to annual fluctuations in lowest low tides. These three residual plots of the HLS records show the HLS fluctuations. The 2σ standard deviations are +/- 2.6 cm at Bai, +/-2.7cm at Sambulaling, and +/-2.8 cm at Angsa. The average HLS uncertainty is +/- 2.7 cm. This is the uncertainty that we can assign assign then to uneroded HLS records. Bai and Sambulaling data are from Fig. 3.42 and 3.50 respectively.

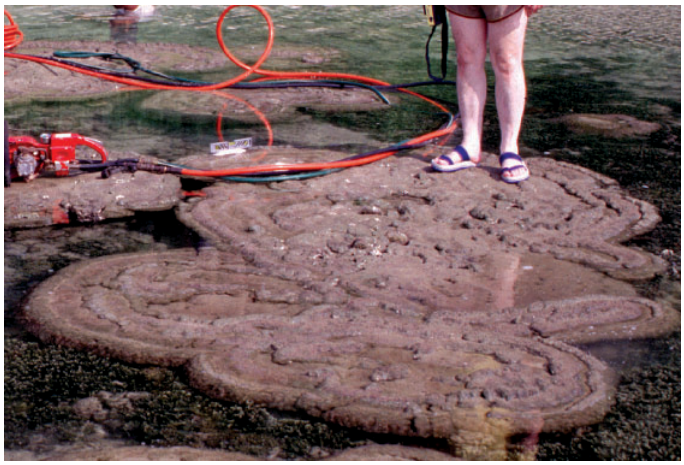

Figure 4.4b Angsa site. During our visit in mid-1997, numerous living microatolls showed pristine micro-topography on their upper surface, characterized by alternating concentric ridges and swales.

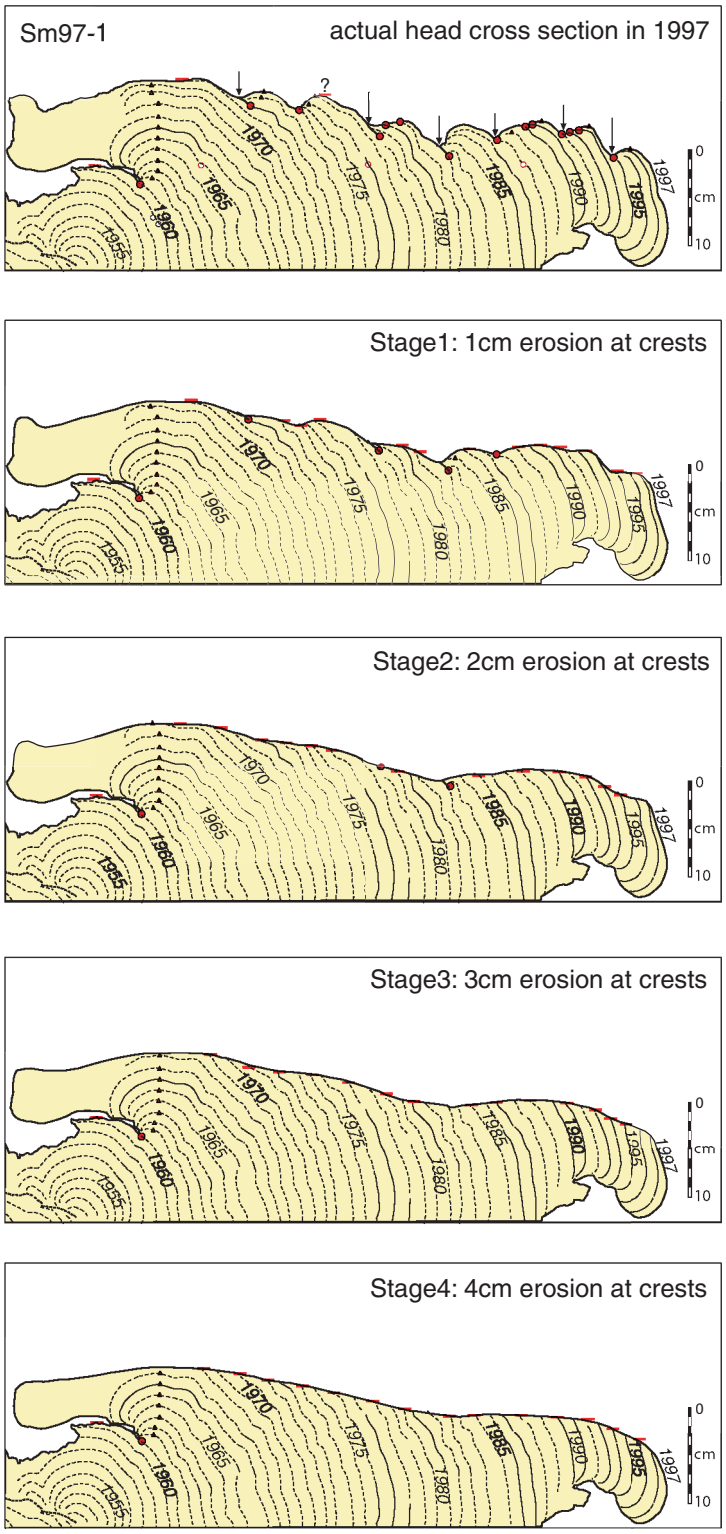

Figure 4.5 Erosions adds additional uncertainty to the rate calculations. These five figures show a hyphothetical degradation of a coral surface assuming erosion occurs predominantly as a diffusive process. The ridges erode more rapidly than swales, because of their more exposed position and greater ratio of surface area to volume.

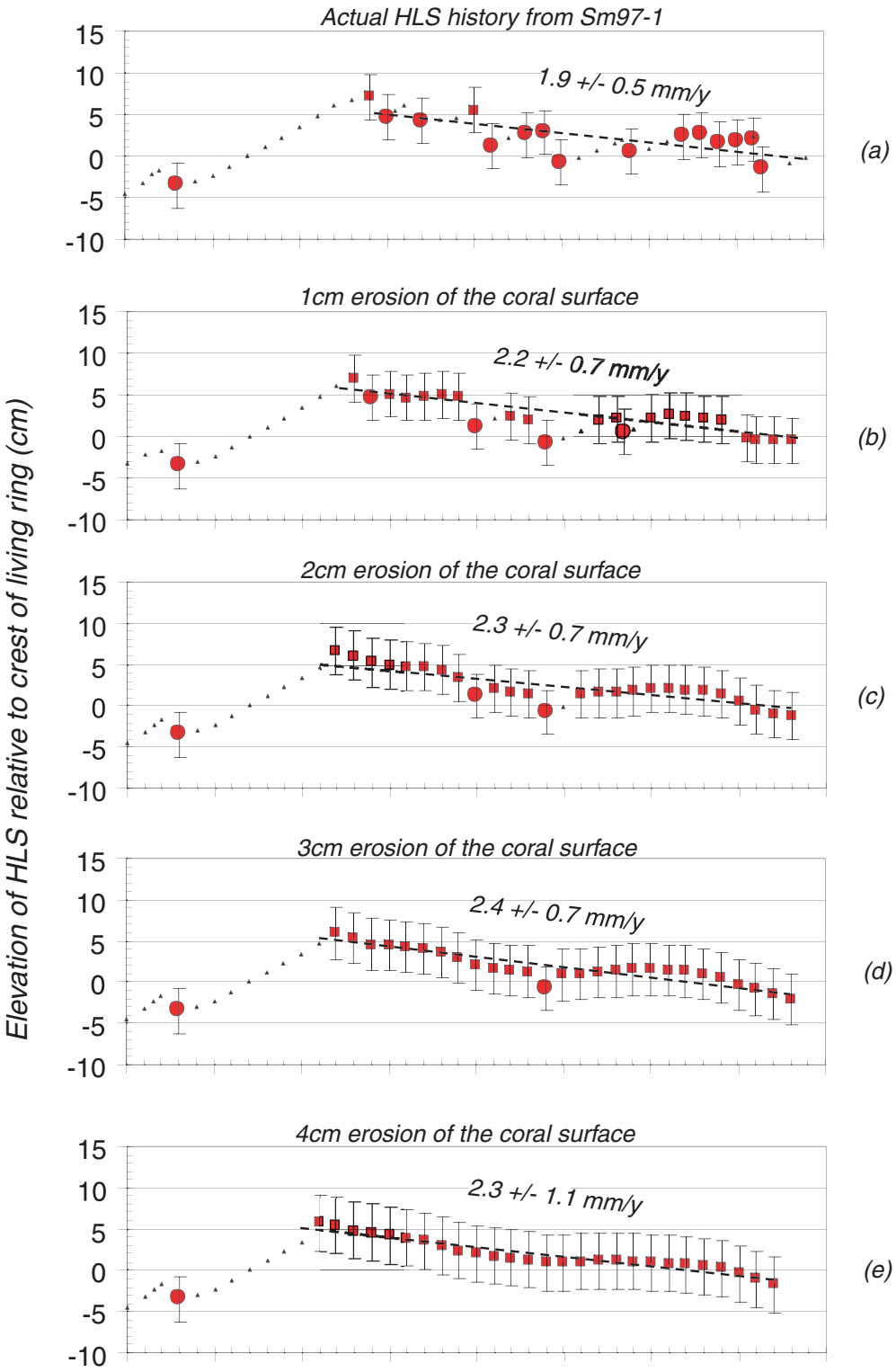

Figure 4.6 Graphical representations of coral degradations shown in the previous figure. The standard errors of the averaged vertical motion rates are calculated using the weighted-least-squared method described in the text. The assigned uncertainties of the 2-σ HLS records are proportional to the severity of erosion.

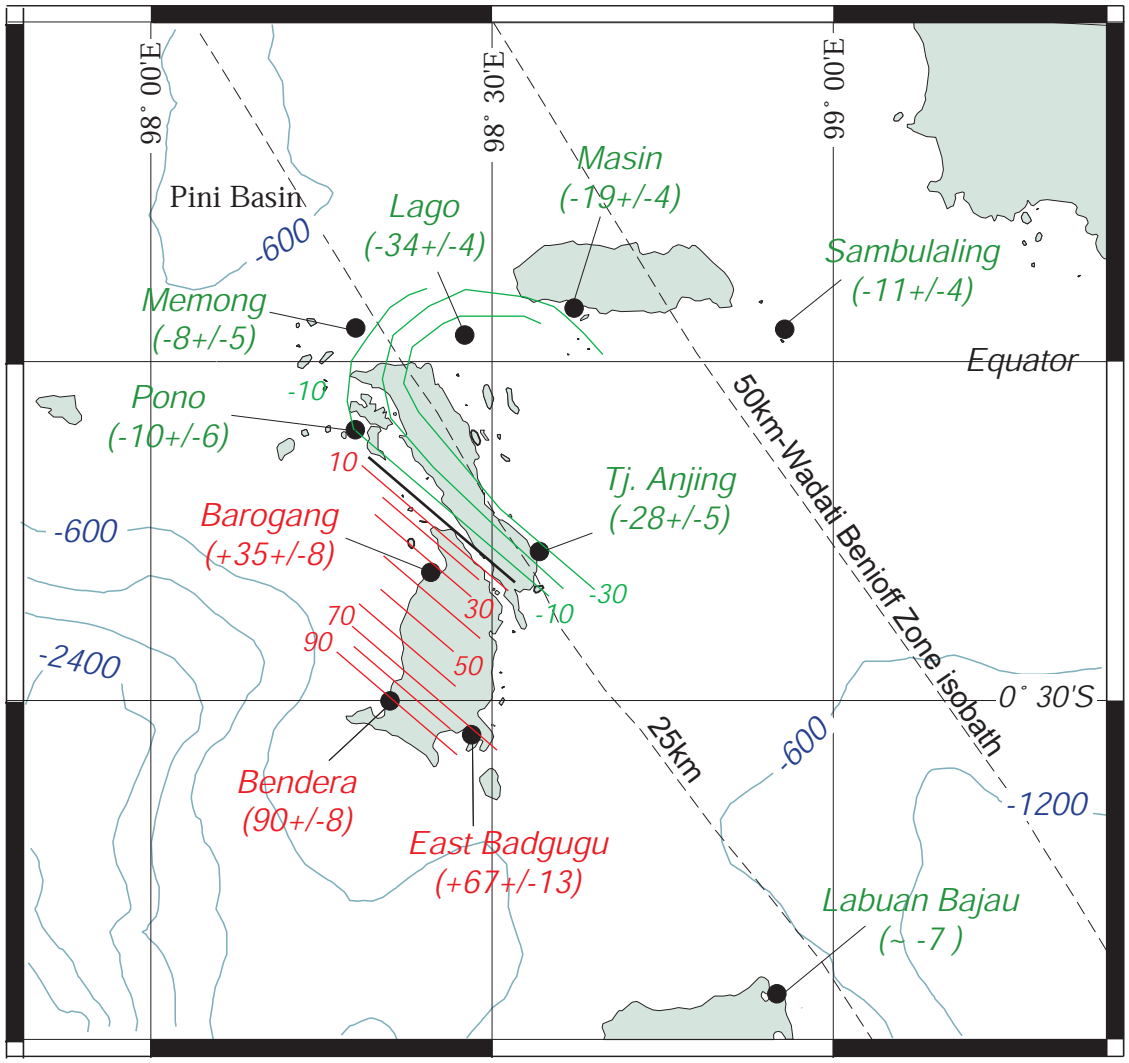

Figure 4.7 Vertical displacements during the 1935 event. The values of emergence (red) and submergence (green) are in cm and are plotted with their 2-σ uncertainty. The red and green lines are contours of the values. Contours of bathymetry (blue) are in meters. The 25-km isobath of the subduction interface cuts diagonaly accross the map.

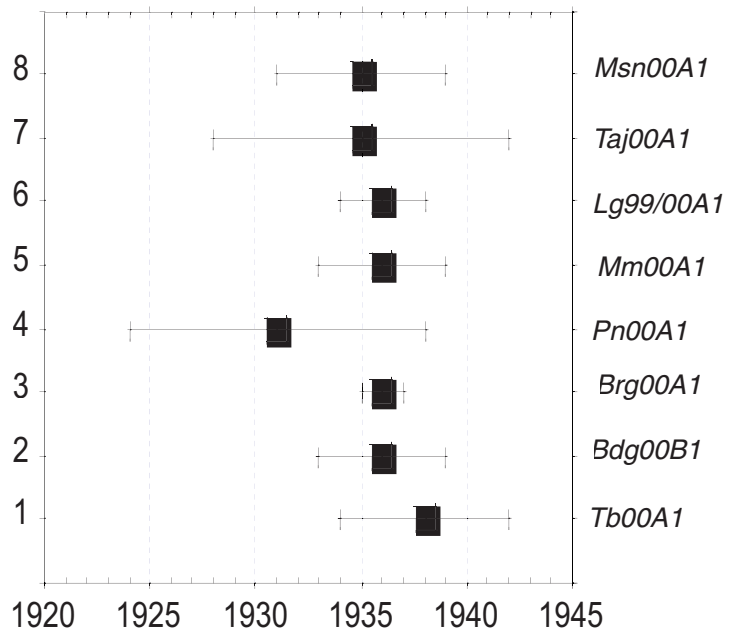

Figure 4.8 Date ranges of the December 1935 event based on visual ring counting from the exterior ring. The weighted average of the dates is 1935.8 +/-0.6 (2σ).

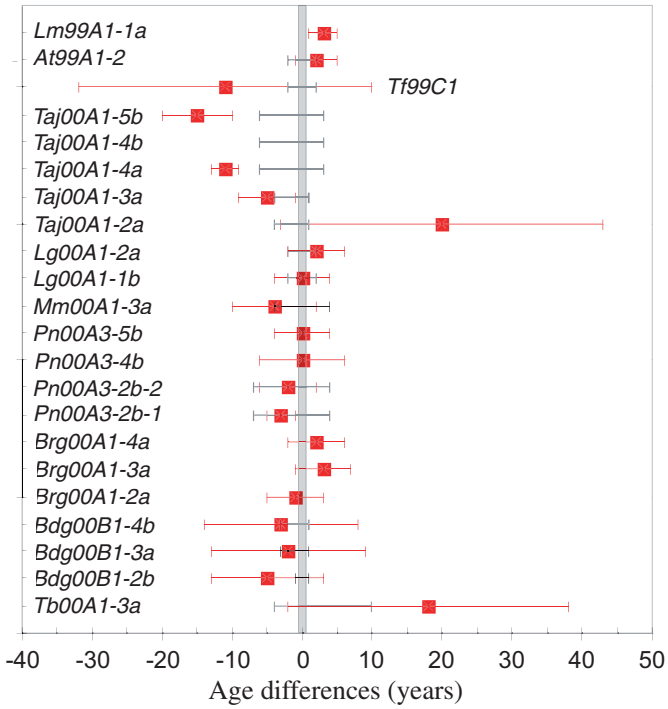

Figure 4.9 Date ranges for the 1935 event, based upon U-Th dates (red squares) and their 2σ uncertainties (red bars) compared to the assigned ages from the visual ring counting (bold gray line with gray bars).

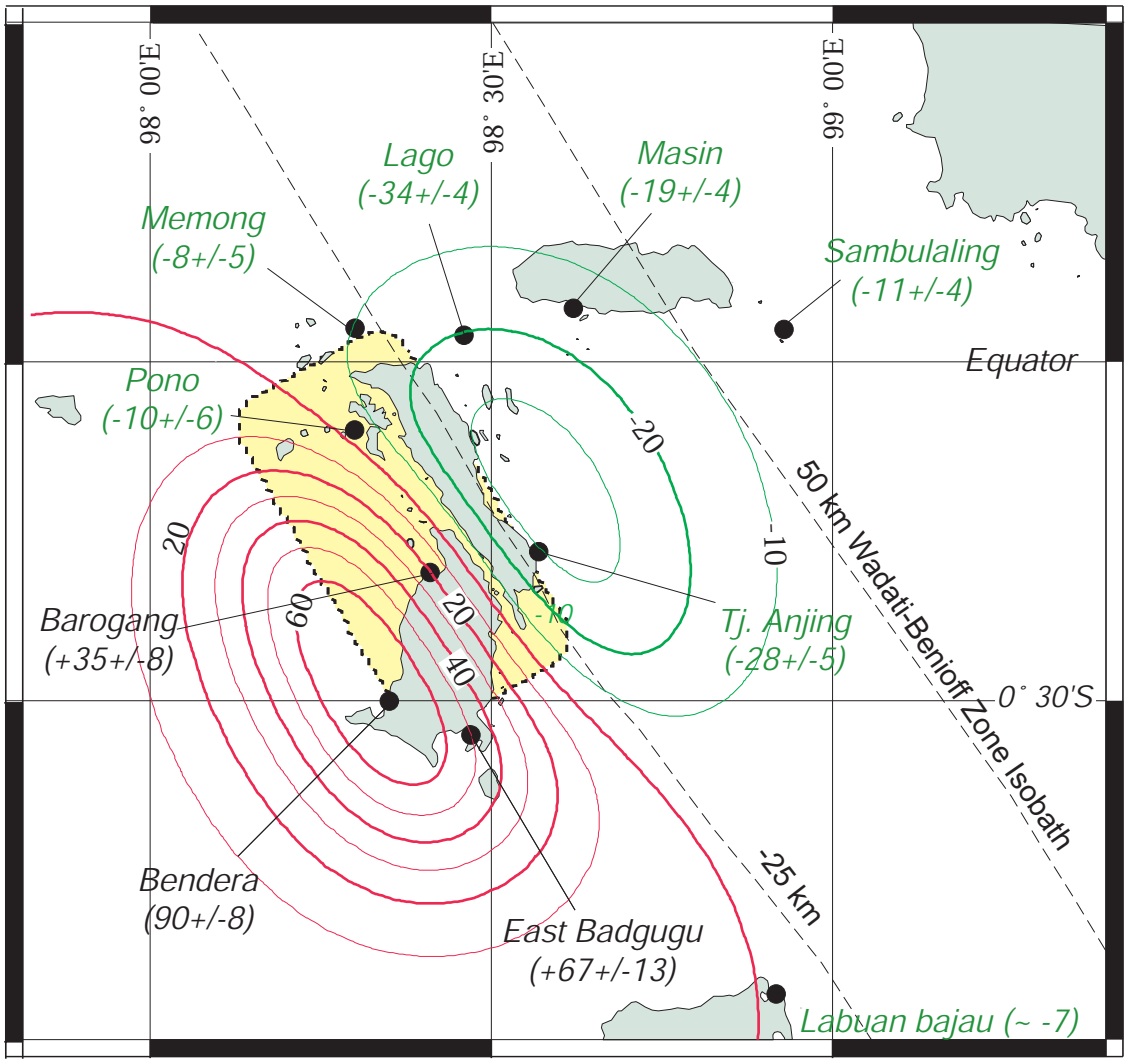

Figure 4.10 A comparison of vertical deformations for the 1935 event. Values plotted under site names are from analysis of our microatoll records. Contours are from elastic dislocation model derived from seismologic rupture parameters, and the yellow rectangle is the seismologically determined source in plan view from *Rivera et al.* [2002].

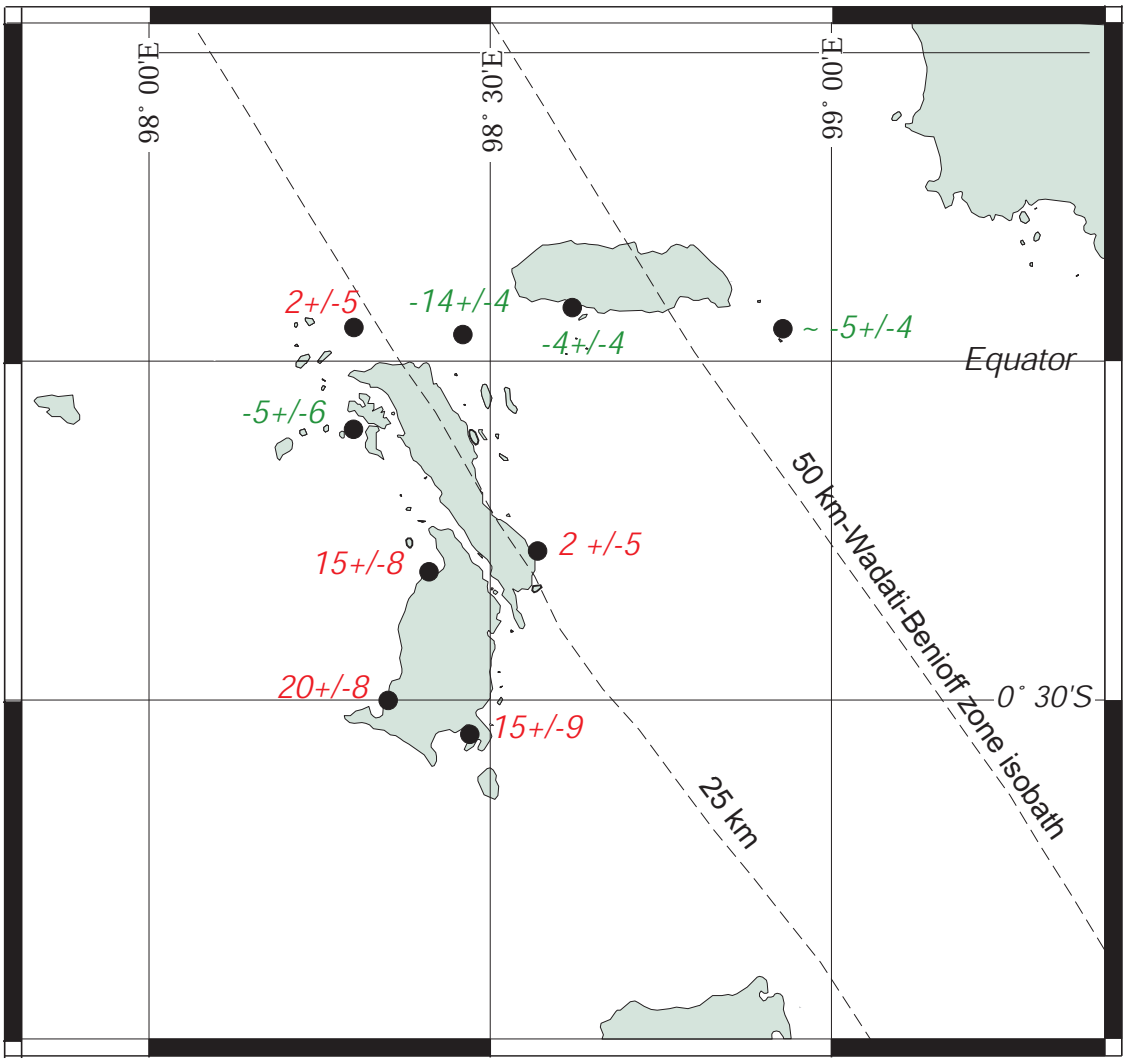

Figure 4.11 Difference between measured uplift determined from microatolls and the uplift predicted by the elastic dislocation model. In general, the measured values of both emergence and submergence are greater than the predicted values. This may mean that significant aseismic afterslip occurred soon after the earthquake.

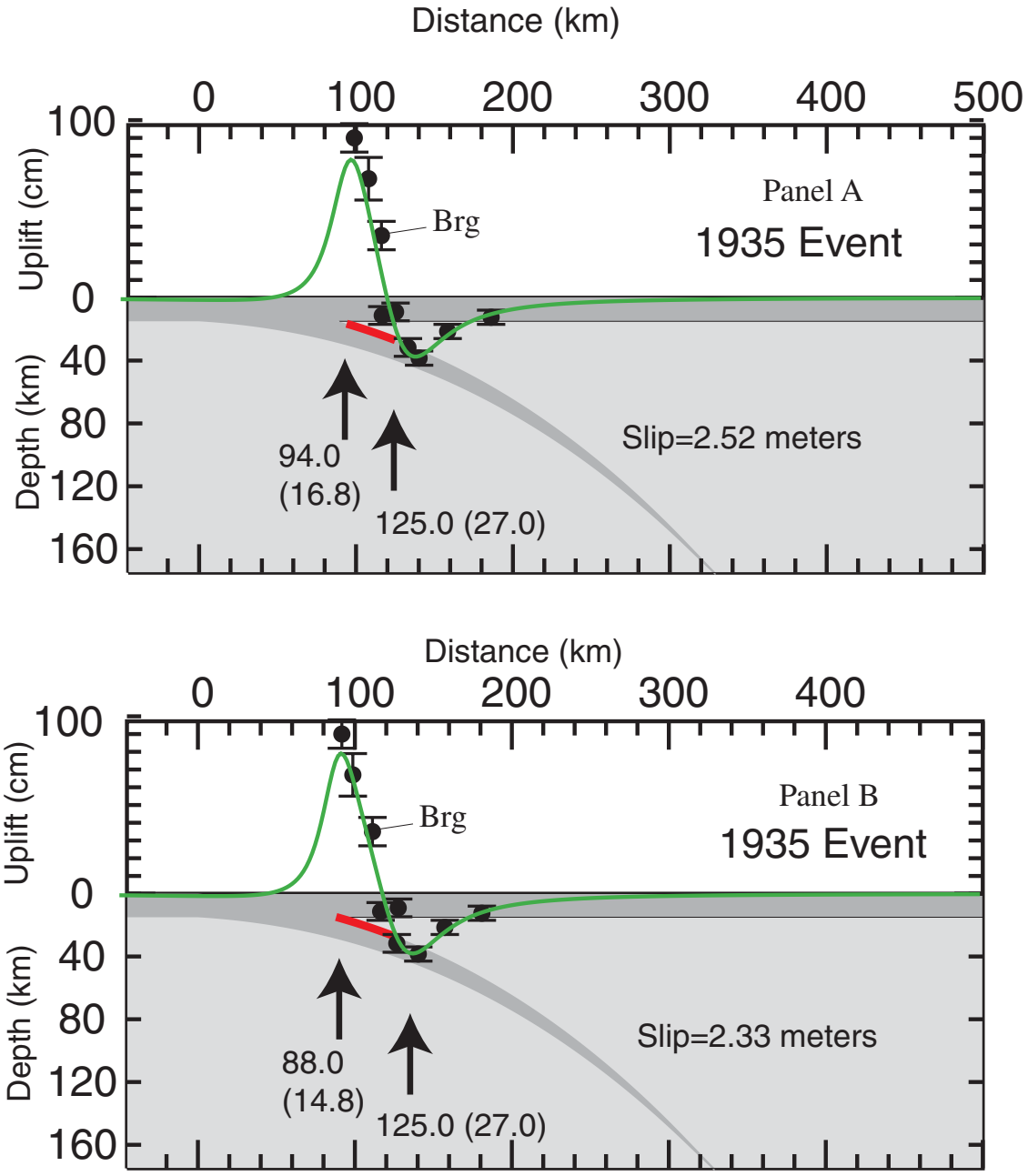

Figure 4.12 2-D fit to microatoll data for the 1935 event. In Panel A the data are projected onto a cross section perpendicular to the trench axis. In Panel B the data are projected onto a cross section drawn 10 degree counter-clockwise from the line perpendicular to the trench axis. Black numbers with arrows are the distance from the trench and the depth to the Wadati-Benioff zone (in kilometers) of the updip and downdip limits of the 1935 rupture patch.

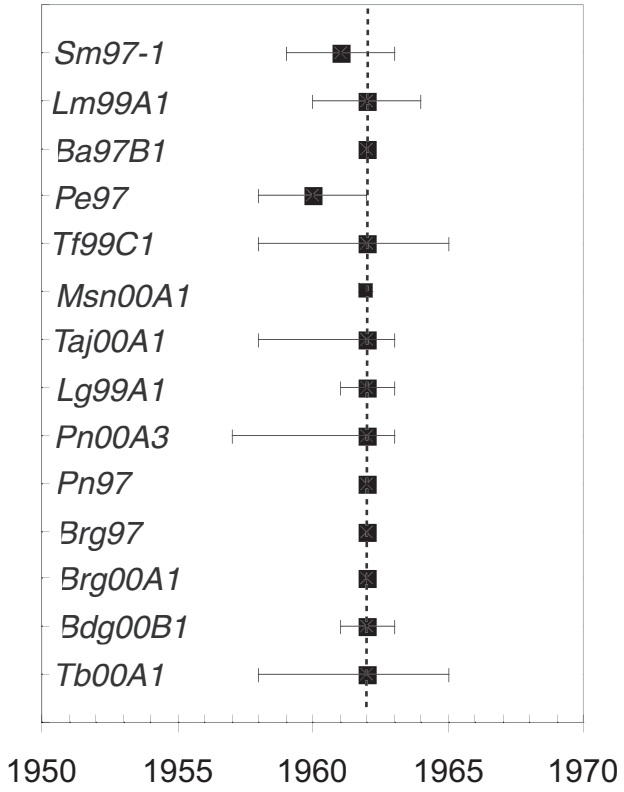

Figure 4.13 Date ranges for the 1962 event based on visual ring counting.

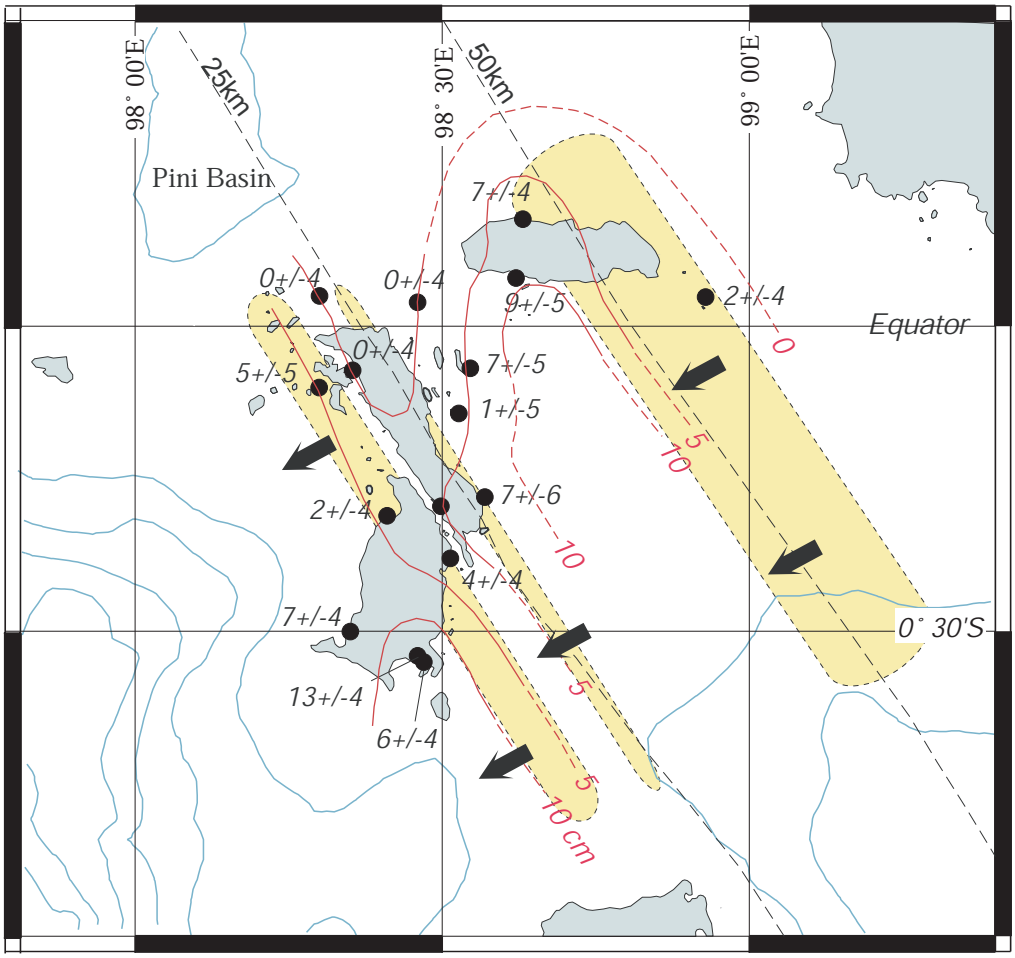

Figure 4.14 Map of emergence event that occurred in 1962. Values are in centimeters. Though coverage is incomplete the contours of uplift suggest two NE-trending ridges of emergence. Yellow shaded patches with dashed boundaries suggest which section of the subduction interface might have slipped to produce the pattern of uplift. Arrows indicate directions of slips.

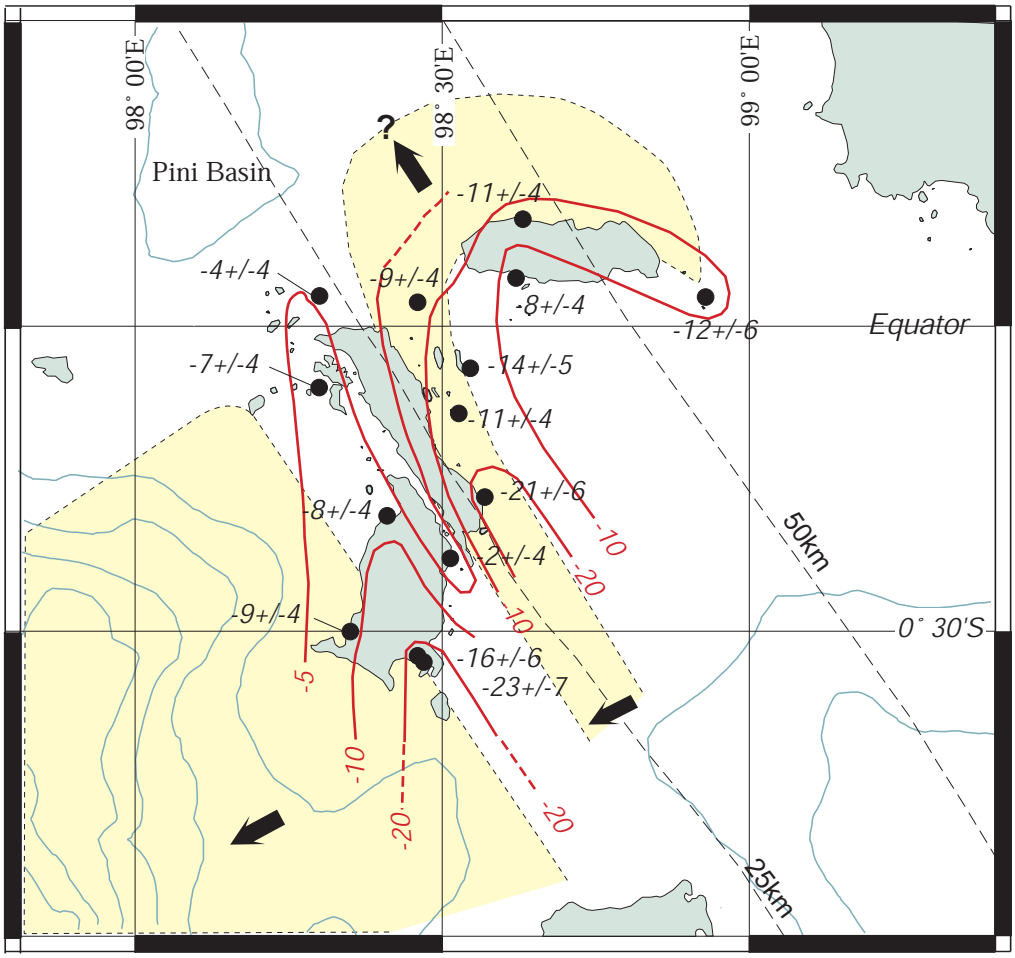

Figure 4.15 Submergence that occurred in 1962 (values in centimeters). The pattern of the submergence, as delineated by the red contours, suggests slip on those patches of the subduction interface that did not slip in the preceding emergence event.

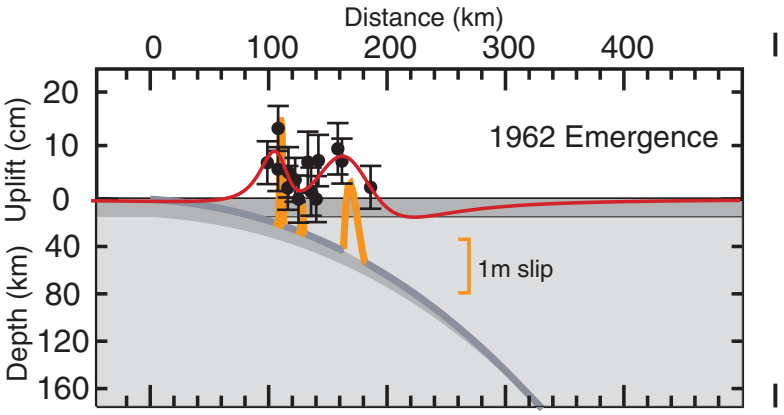

Figure 4.16 The 2-D elastic dislocation fit of the paleogeodetic data of the 1962 emergence event. Slips are allowed to vary along the patch. The observed emergences are explained by slips on and near the lower boundary of the 1935 patch and on a wider patch further down-dip. Black dots and vertical bars represent values of paleoseismic emergence with their 2-σ errors. The scatter of the data reflects their variability along strike. Red bars indicate the sections of the subduction interface that slipped. Bold orange lines show the magnitude of slips on the subduction interface prescribed by the inversion. The triangular shape of the orange line indicates that we have allowed slip to vary on the interface. The thin red curve is the modeled vertical surface deformation.

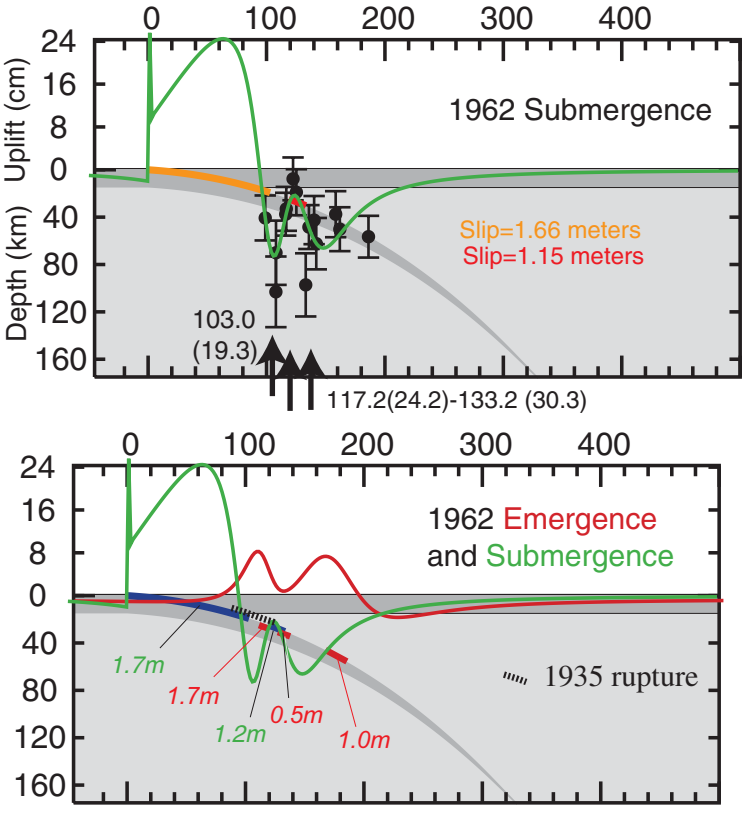

Figure 4.17 Data of the 1962 submergence are predicted by slips on the outboard patch of the 1935 rupture and on the narrow patch near the down-dip edge of the 1935 slip source. Scattering of the data may suggest slip variations along the strike. Uniform slips of 1.7 m on the orange patch and 1.2 m on the red patch produce the double-troughed deformation pattern shown in green. The model curve fits much of the data, but the two extreme submergence values are grossly underfitted.

Figure 4.18 Superposition of the slips on the subduction interface from the 2-D elastic dislocation models of 4.16 and 4.17. The 1962 slip patches overlap with the 1935 rupture but extend farther up-dip and down-dip. This may indicate that the 1962 silent event facilitates the distribution of slips throughout the broader interface.

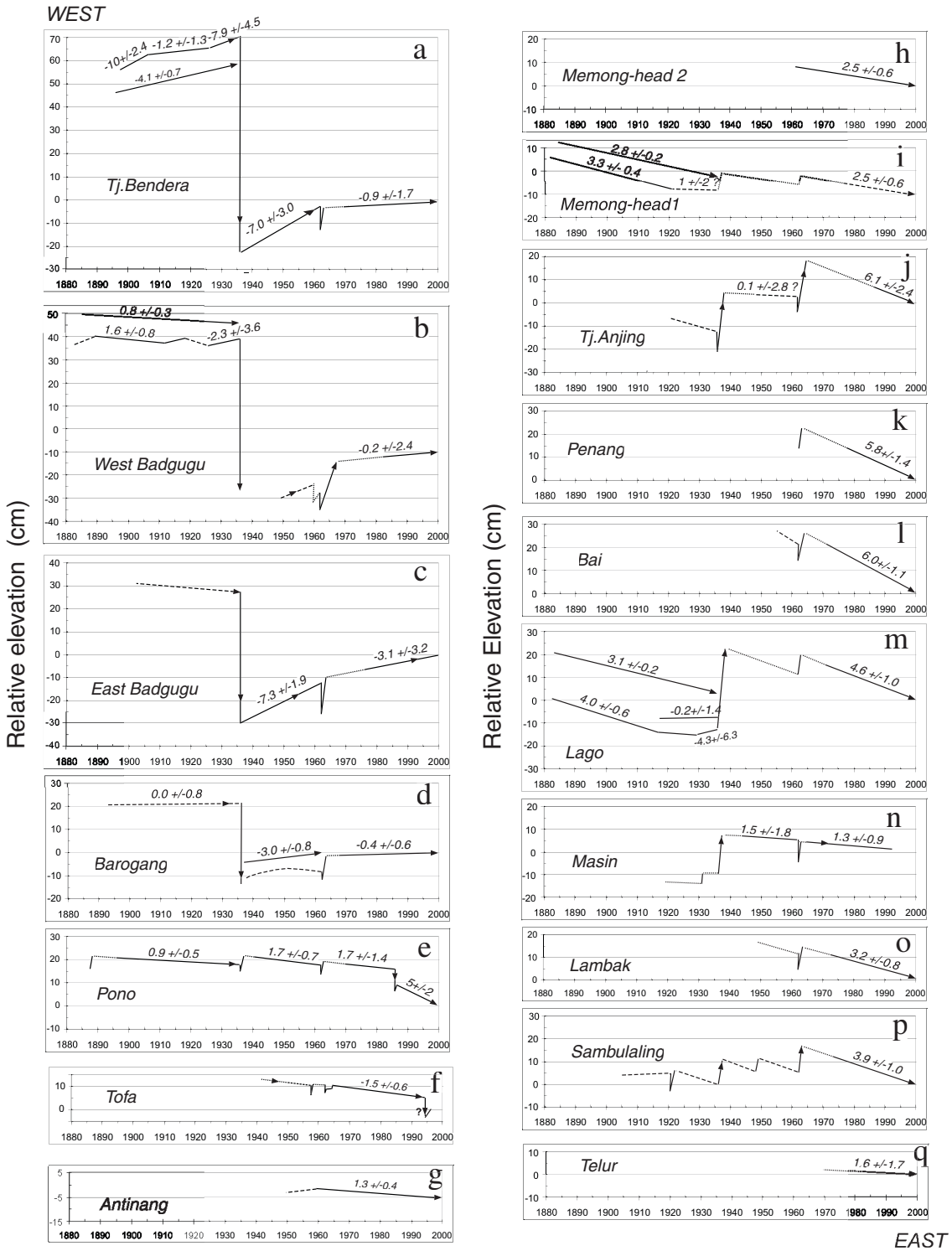

Figure 4.19 Paleogeodetic records derived from HLS records, but corrected for a 2 mm/yr global glacio-hydro-isostatic sea-level rise.

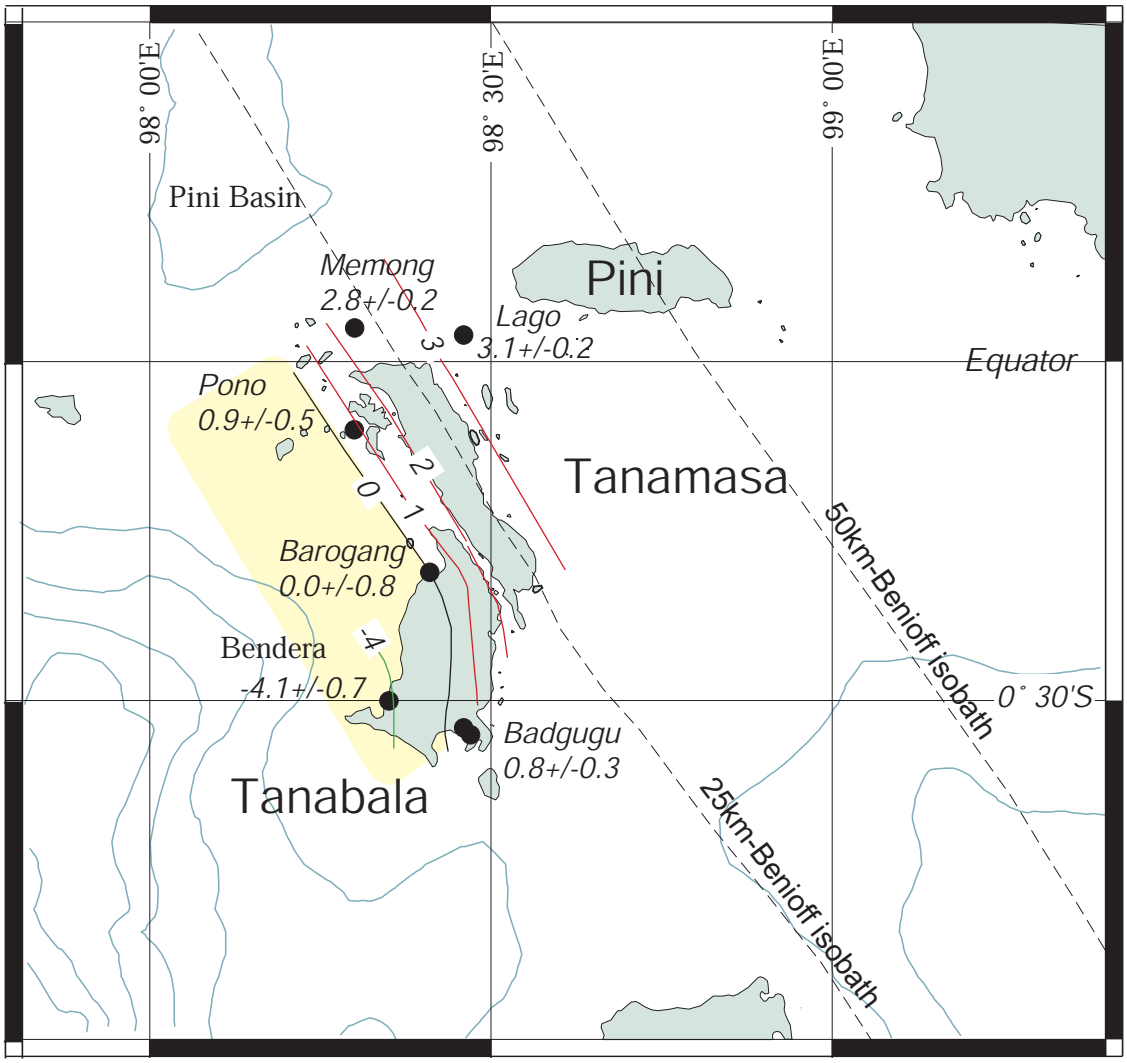

Figure 4.20 Rates of slow vertical deformation prior to 1935, adjusted for 2 mm/y of the global sea level rise. Shaded domain is the region that was slowly submerging. The highest recorded submergence was ~4 mm/yr. Eastern part of the islands was emerging. The highest emergence was ~3 mm/yr

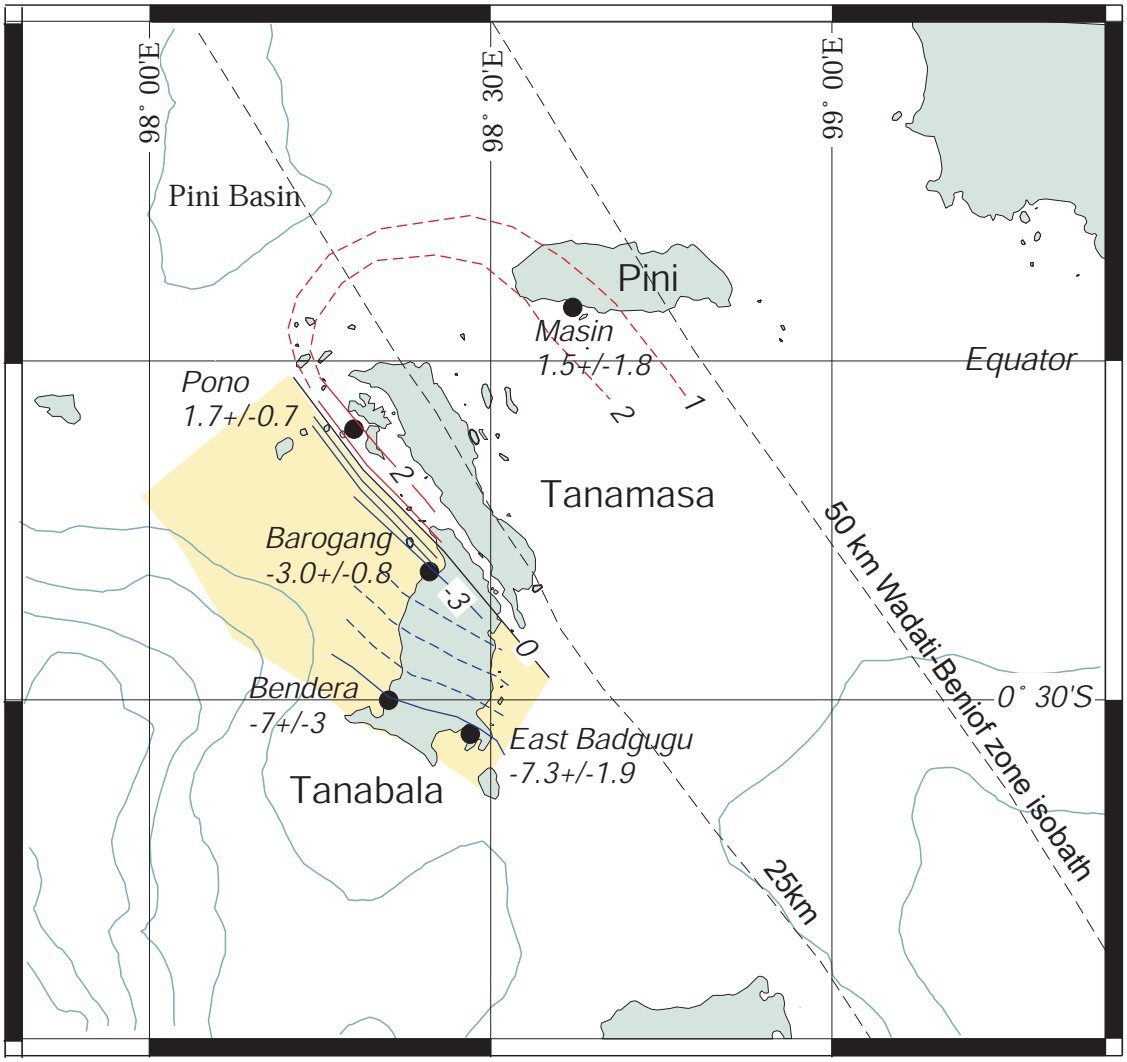

Figure 4.21 Average rates (mm/y) of post-seismic deformation from 1935 to 1961 after a rate adjustment by 2 mm/yr for global sea-level rise (data from Fig.4.19). Submergence rates of the sites in the western part abruptly increased. The highest recorded submergence is 7 mm/yr.

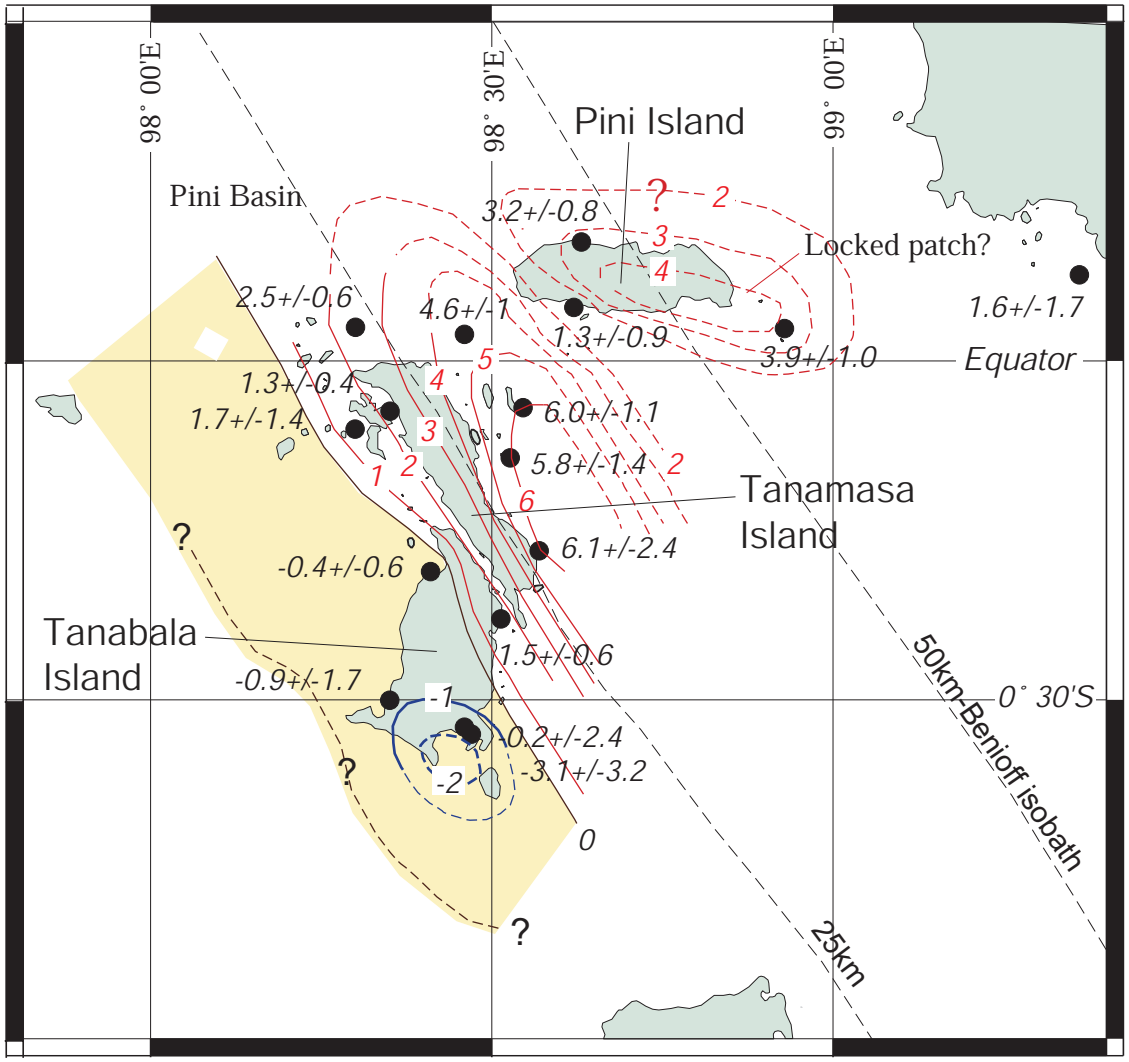

Figure 4.22 Modern rates (1962-2000) after 2 mm/yr adjustments for the global sea-level rise. Values are in milimeters per year. Contouring of the values shows that the hingeline runs parallel to the trench. The maximum submergence occurs around the southwestern part of Tanabala Island. The larger maximum emergence is centered about 10 km off the east coast of Tanamasa Island. An "odd" ridge of emergence runs almost parallel to the long axis of Pini Island.

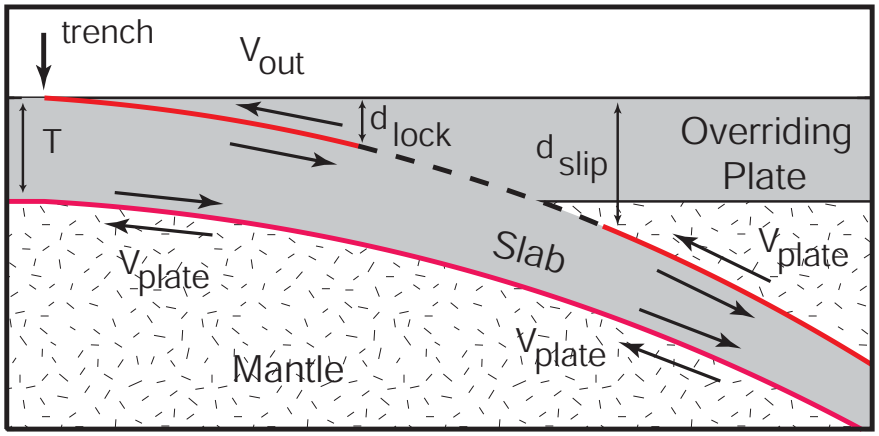

Figure 4.23a Sketch showing the parameters of an idealized elastic dislocation model of interseismic deformation at a subduction zone [*after Sieh et al.*, 1999]

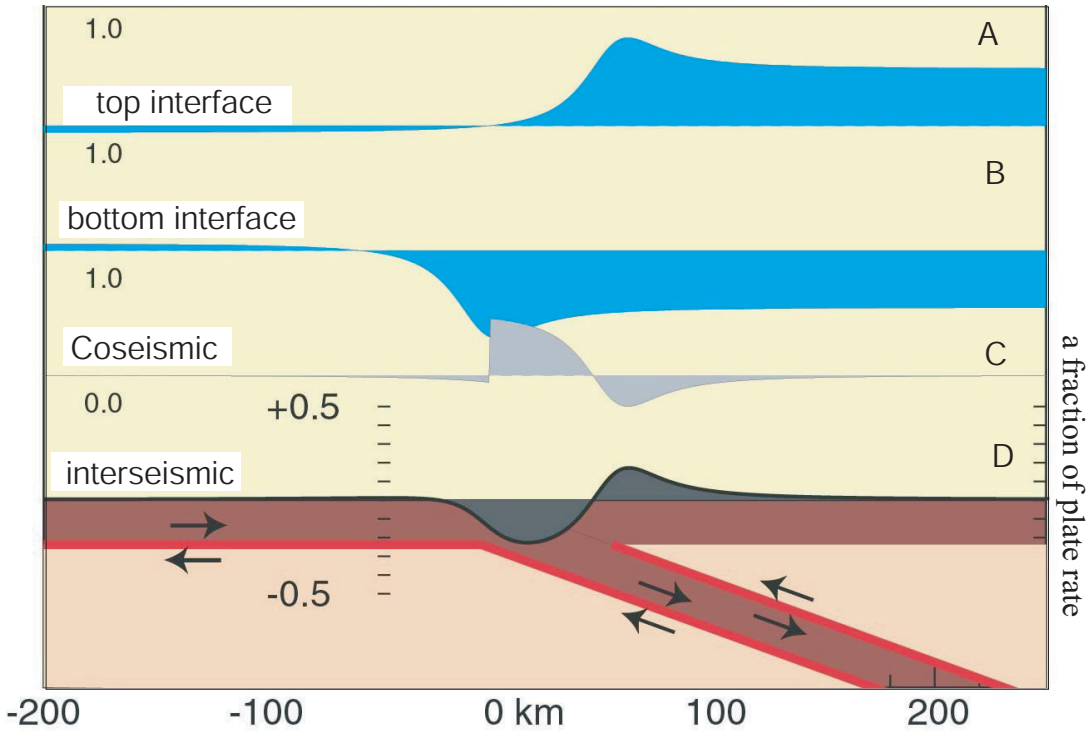

Figure 4.23b An elastic dislocation model of an earthquake cycle. Red patches slip equal to a plate rate (i.e. a fraction of aseismic slip is 1.0) during an interseismic period. Panels A and B show contributions to vertical motion from indivdual sources. Panel D shows a total vertical motions. Note that motions due to the top and the bottom interfaces are nearly mirror image to each other. So, in a steady state subduction they nearly cancel one another. Panel C shows vertical motion in a seismic event, which is nearly a mirror image to that of the interseismic period [*from Steve Ward, written comm.,* 2002].

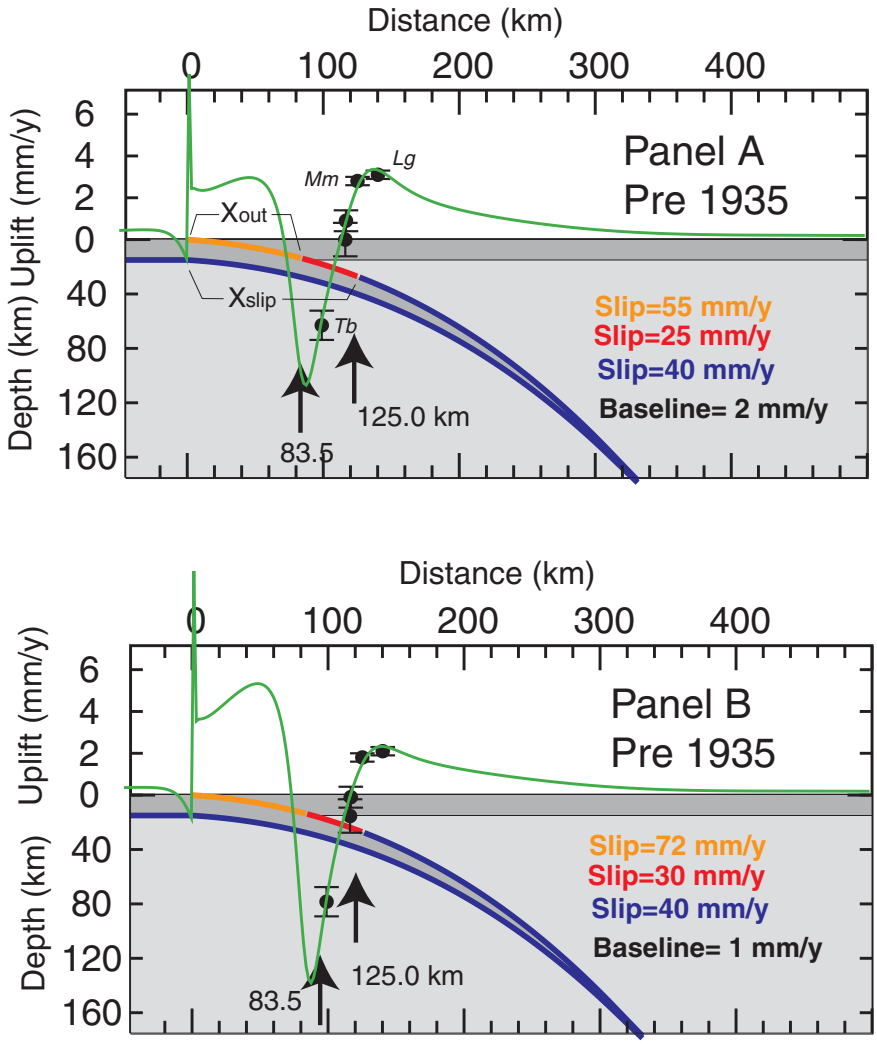

Figure 4.24 Elastic dislocation models of slow vertical deformation prior to 1935. Panel A uses a 2 mm/y global sea level rise correction. Panel B assumes 1 mm/y. The high rate of submergence and low rates of emergence require rates of slip on the subjacent interface that are 50 -75% of the long-term plate rate. Slip rates on the interface between the islands and the trench are appreciably higher than the long-term plate rate.

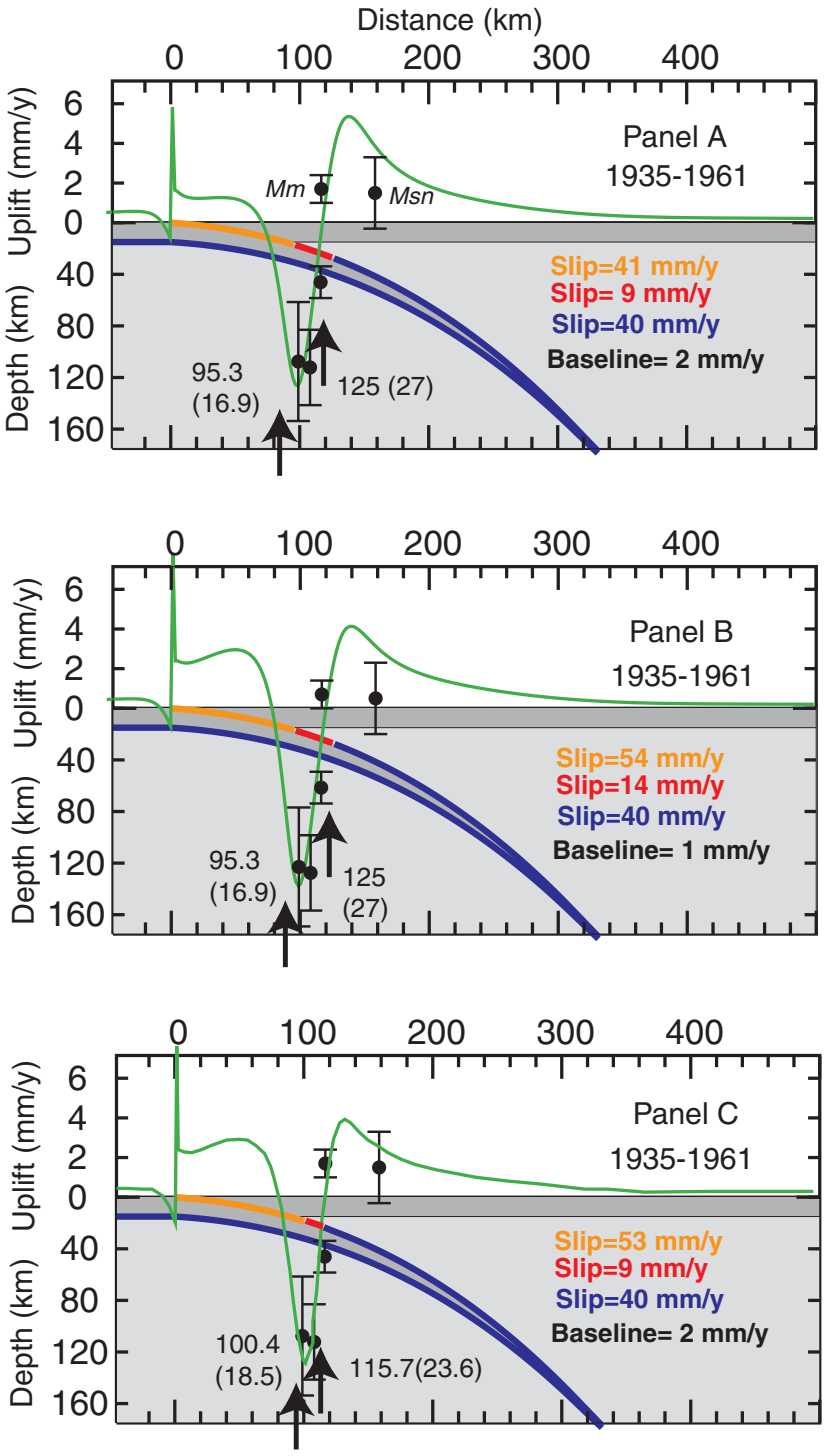

Figure 4.25 Elastic dislocations modeling of slow vertical deformation for the period from 1935 to 1961. Paleogeodetic data are projected onto a cross-section perpendicular to the trench. Both Panel A and B have a fixed boundary at 125km from the trench but use a global sea-level rise correction of 2 mm/yr and 1 mm/yr respectively. In Panel C this boundary has been allowed to move. In all three models the up-dip section slips at or slightly faster than long-term plate rate. Data from the western part require the 1935 rupture patch to creep at about a quarter of the long-term plate rate. Panel C shows that intrusions of the creeping up-dip and down-dip sections into the healed 1935 rupture patch better fit the eastern data.

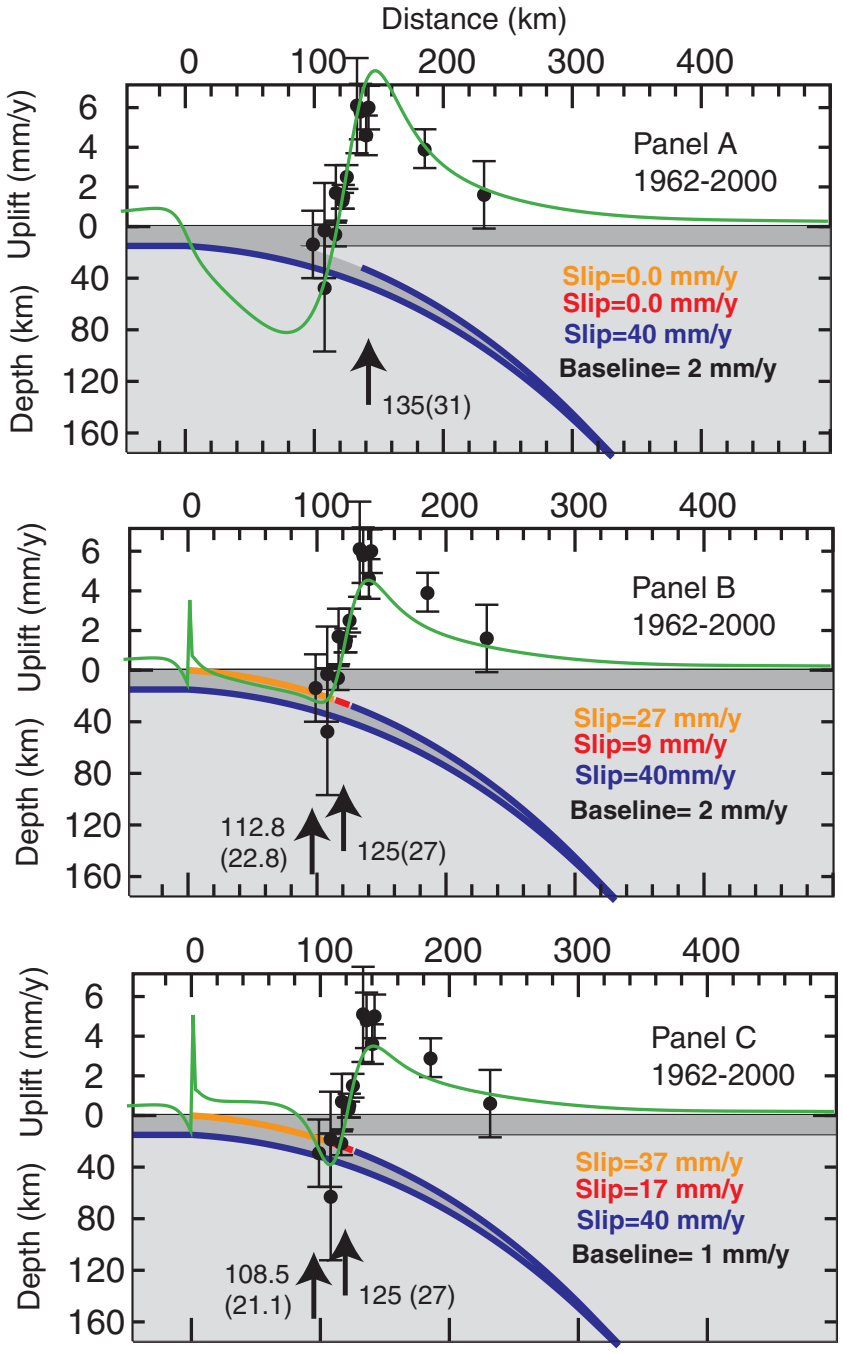

Figure 4.26 The 2-D inverse elastic dislocation models of the modern rates (1962-2000). The fully locked model in Panel A is an acceptable inverse model, but greatly under predicts the important westernmost point. Models in Panel B and C fit the westernmost point and thus are preferred solutions. The principal observation is that the submergence rates in the western part have declined significantly since 1962. This requires that slip rates on the interface between the island and the trench have decelerated to only about 65% of the long-term plate rate, but that the zone of slippage extent farther down-dip onto the principal locked patch.

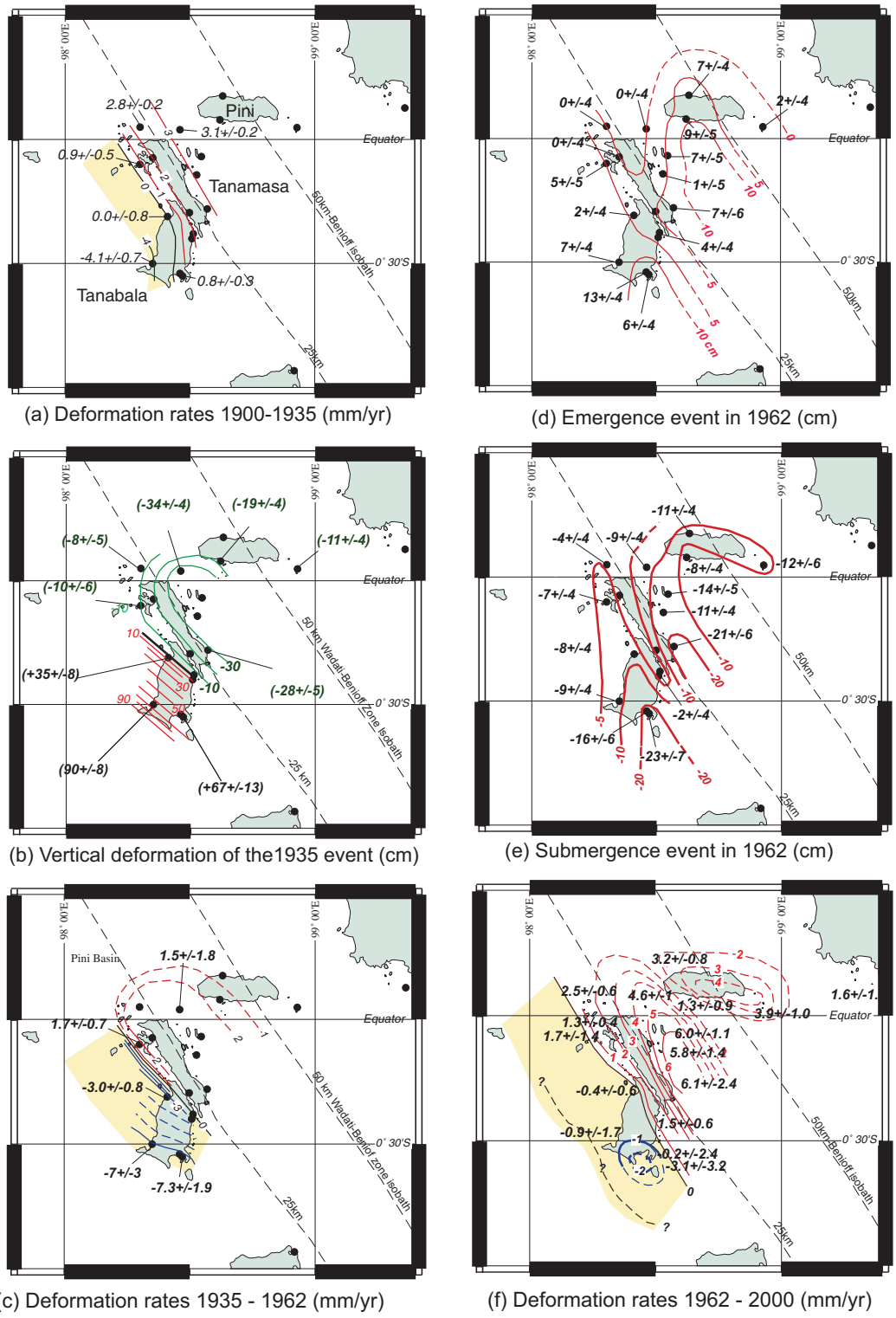

Figure 4.27 Summary of paleogeodetic records of vertical deformations for the 20th century. Note that deformation rates differ significantly between the three periods separated by the 1935 and 1962 events. Submergence rates are fastest in the post-earthquake period 1935-1962. In the past four decades the rates slowed down. These differences indicate changes in the the slip rates and other processes operating on and around the subduction interface.

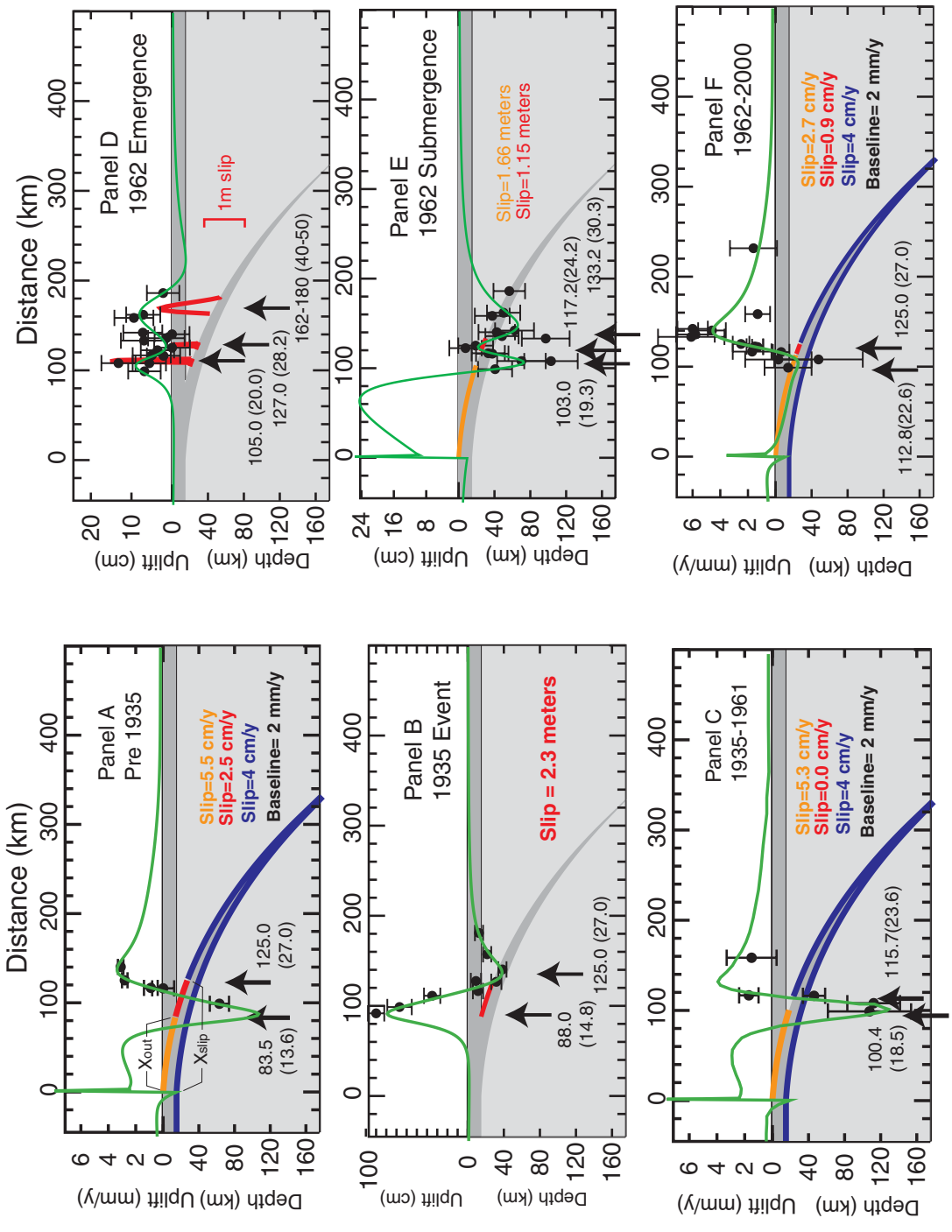

Figure 4.28 Summary of the elastic dislocation models of the century-long paleogeodetic history. The 1935 and the 1962 are the major tectonic events, and demarcate appreciable changes in the behaviors of the subduction interface.

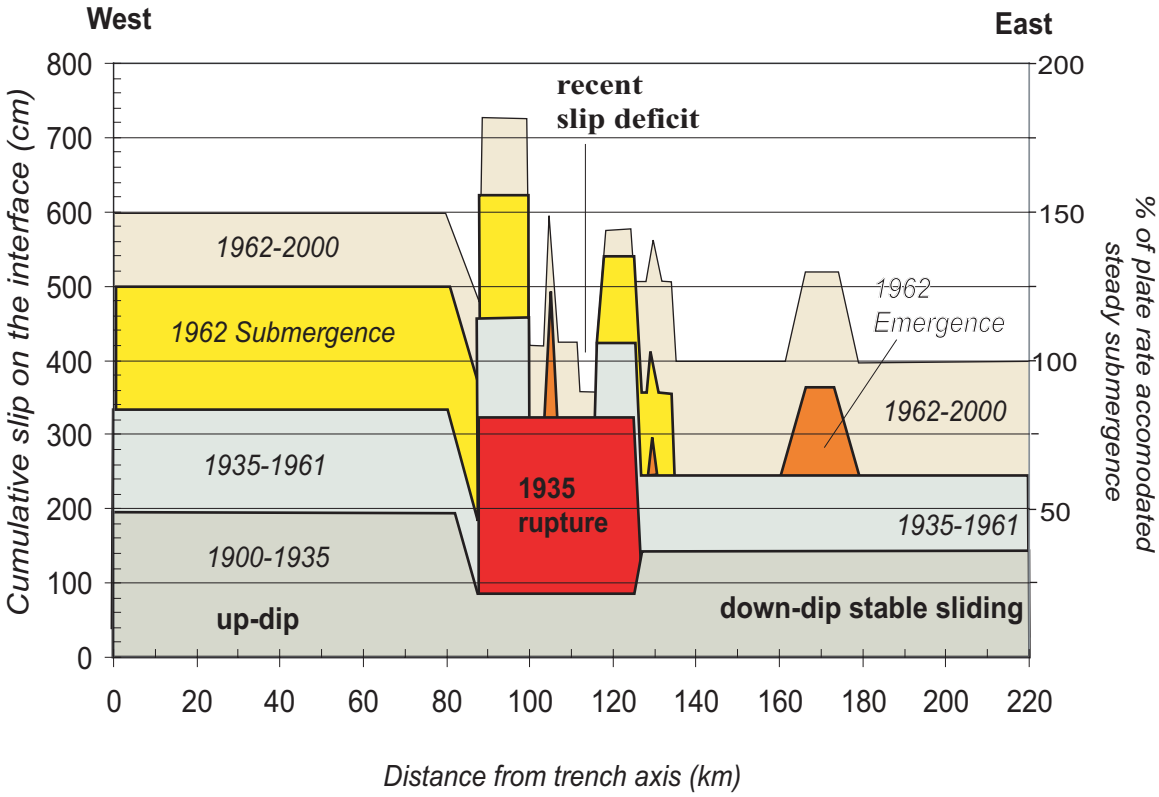

Figure 4.29 Seismic and aseismic slip history on the subduction interface from 1900 to 2000 based on paleogeodetic data and elastic dislocation models. The red, yellow, and green areas represent the amount of slips in the 1935, 1962 emergence, and 1962 submergence events respectively. All other colors represent aseismic slips during intervening periods. Stable sliding at plate rate is indicated as 100% on the right-side scale.

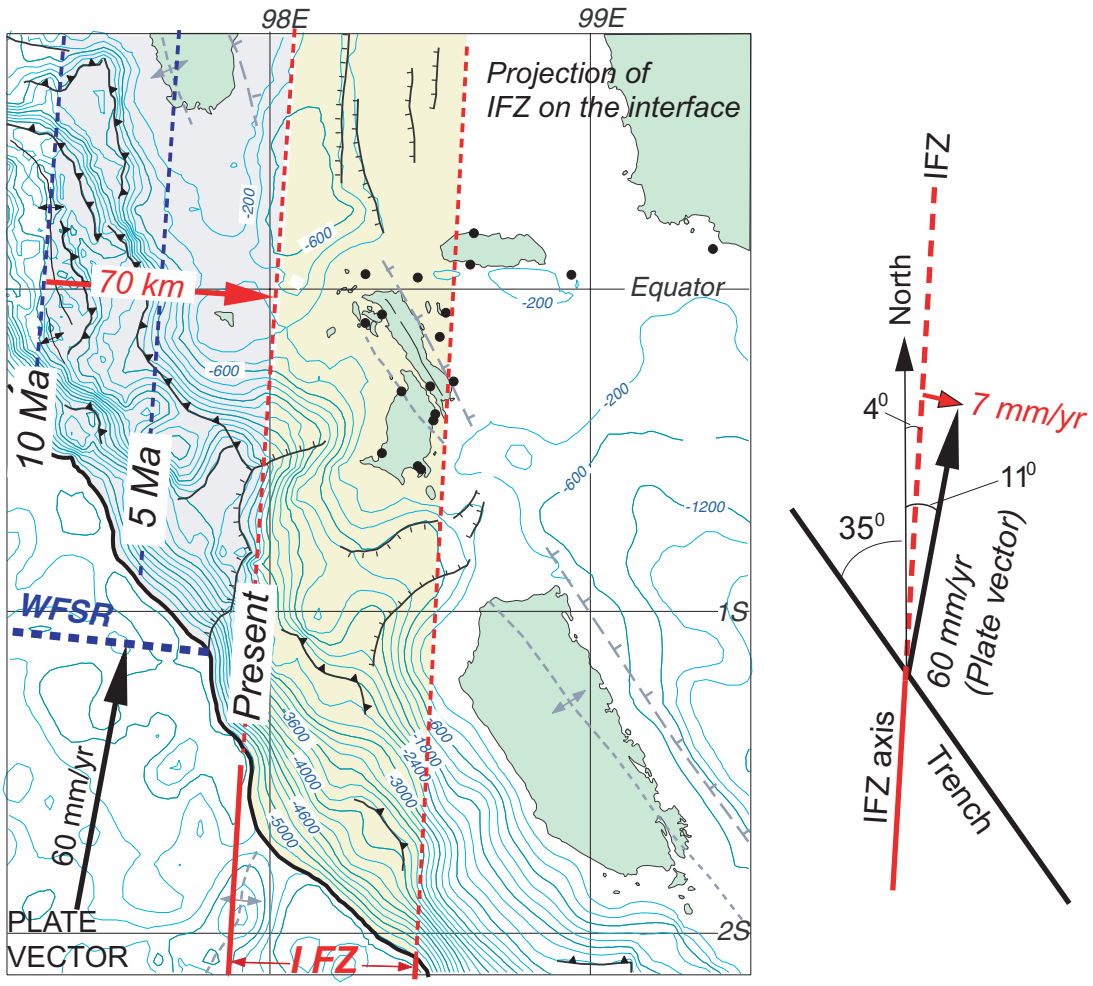

Figure 4.30. Hyphothesis of the eastward moving of the subducting Investigator Fracture Ridge zone (IFZ) along the Sumatran subduction. WFSR is Wharton Fossil Spreading Ridge zone. The plate vector is ~7 degree eastward from the axis of the IFZ. Thus, the IFZ moves toward east about 7 mm/yr. The IFZ moved about 70 km since 10 Ma or about 155 km along the trench axis. This subducting IFZ may have led to the intense faulting on the hanging wall above and to the high percentage of aseismic slip on the subduction interface. Gray shaded and yellow shaded regions indicate the trails of and an approximate present position of the IFZ.